AGU ADVANCING EARTH AND SPACE SCIENCE

Water Resources Research

RESEARCH ARTICLE
10.1029/2021WR030847

Response of Flow and Saltating Particle Characteristics to Bed Roughness and Particle Spatial Density

Chenwei Zhao[1], Pablo Ouro[2], Thorsten Stoesser[3], Subhasish Dey[4], and Hongwei Fang[1]

[1]Department of Hydraulic Engineering, State Key Laboratory of Hydro-science and Engineering, Tsinghua University, Beijing, China, [2]Department of Mechanical, Aerospace and Civil Engineering, The University of Manchester, Manchester, UK, [3]School of Civil, Environmental and Geomatic Engineering, Engineering Fluid Dynamics Research Centre, University College London, London, UK, [4]Department of Civil Engineering, Indian Institute of Technology Kharagpur, Kharagpur, India

Key Points:

- A numerical model combining large-eddy simulation and point-particle methods is employed for tracking particle trajectories
- The effects of bed roughness and particle spatial density on the bedload transport are investigated by numerical simulations
- Both kurtosis and skewness of the distributions of key saltation parameters change due to an increase in bed roughness

Correspondence to:
H. W. Fang,
fanghw@mail.tsinghua.edu.cn

Citation:
Zhao, C. W., Ouro, P., Stoesser, T., Dey, S., & Fang, H. W. (2022). Response of flow and saltating particle characteristics to bed roughness and particle spatial density. *Water Resources Research*, *58*, e2021WR030847. https://doi.org/10.1029/2021WR030847

Received 16 JUL 2021
Accepted 4 MAR 2022

Abstract With the goal to explore the effects of natural bed roughness on bedload transport, numerical simulations of flow and particle saltation are carried out with varying bed roughness and particle spatial density. A combination of Eulerian and Lagrangian point-particle methods is applied to solve the equations of motion of the fluid and the particles within the large-eddy simulation framework. Flows over smooth and rough beds with four particle densities are considered. As the bed roughness increases, there is a leftward shift of the double-averaged streamwise velocity profiles against dimensionless vertical distance, which is scaled with the bed roughness height, an upward shift of the peak values of double-averaged Reynolds stresses, and a fragmentation and disappearance of coherent structures in the form of high-speed and low-speed near-bed streaks. These observations are consistent with those of previous studies. As the bed roughness increases, the mean resting time of saltating particles increases, however the particles' saltation length, velocity, and angular velocity decrease, while their saltation height remains almost unchanged. Saltation height, saltation length, particle angular velocity, and resting time exhibit linear, gamma, normal, and exponential distributions, respectively. Further, as the bed roughness increases, the kurtosis and skewness of some particle parameters vary, and the particle velocity shifts from a symmetrical normal to an asymmetrical gamma distribution.

1. Introduction

Bedload transport refers to the conveyance of sediment particles within a few particle diameters of the sediment bed (Dey, 2014). For some time, this has been a fascinating research topic in fluvial hydraulics, sedimentology, and hydraulic engineering (Durán et al., 2012; Hohermuth & Weitbrecht, 2018; van Rijn, 1984). In a natural stream, especially in mountainous regions, the bedload can contribute up to 60% of the total sediment transport, and thus has a significant impact on the fluvial environment (Lajeunesse et al., 2010; Meunier et al., 2006), pollutant or material transport (Fang et al., 2017; Huang et al., 2015), and habitat alteration (Bui et al., 2019; Pitlick & Van Steeter, 1998). In addition, the morphology of the movable bed in natural streams, before the formation of ripples or dunes, is relatively flat but not smooth. The bed roughness which is essentially introduced to describe the roughness effect of the undulate bed on a fluid flow influences the bedload transport rate. As a consequence, understanding the physical mechanism of sediment transport over the natural rough bed is of fundamental importance in improving the accuracy of bedload transport rate predictions.

In the past couple of decades, a multitude of experimental and numerical studies have explored the characteristic features of bedload transport. In experiments, image recording techniques are widely used to track particle trajectories in laboratory flumes (Abbott & Francis, 1977; Amir et al., 2014; Lee et al., 2000; Niño & García, 1998; Roseberry et al., 2012; Shim & Duan, 2017). However, in most cases, only the statistics of particle motion have been recorded and analyzed, with fluid dynamics analysis neglected because of the difficulties involved in detecting the particle and fluid motions simultaneously (Witz et al., 2019). In numerical simulations, some investigators have described the bedload transport using deterministic and stochastic models based on empirical formulas, such as Bagnold's approach, Einstein's approach, or the Exner equation (Ancey, 2010; Bagnold, 1966; Einstein, 1941; Vowinckel et al., 2016). However, in these cases, only the mean flow values or conditional averaging of turbulent flow structures were utilized, and the effects of instantaneous turbulence on the transport of bedload particles were neglected. In recent years, approaches that combine computational fluid dynamics (CFD) models with the discrete element method (DEM) to resolve particle-laden turbulent flows have become

increasingly popular due to improvement in supercomputing facilities. Models based on direct numerical simulation (DNS), large-eddy simulation (LES), and Reynolds-averaged Navier-Stokes (RANS) models can be used (Ji et al., 2014; Kidanemariam & Uhlmann, 2014; Kuerten, 2016; Mazzuoli et al., 2020; Papanicolaou et al., 2008; Schmeeckle, 2014; Vowinckel et al., 2014; Yousefi et al., 2020). Among them, LES appears to be better suited to the simulation of large Reynolds number turbulent flow and large-scale domain with a great number of particles, in terms of accuracy and computing efficiency. As for DNS simulation it is too time consuming, while RANS simulation may average turbulent flow information. Very few numerical simulations of channel flow with natural rough bed and bedload transport have been reported. For instance, Alfonsi et al. (2019) used an LES model to focus on the turbulent flow generated by a natural rough pebble-bed. Chan-Braun et al. (2011) and Mazzuoli and Uhlmann (2017) performed DNS where they used a layer of spheres to create bed roughness in an open-channel flow and explored the turbulent flow structure around bed-mounted spheres and the forces and torque acting on spheres were quantified. This work was later extended by Vowinckel et al. (2014, 2016) who used loose spherical particles to simulate bedload motion studying the effects of bed roughness (created by the fixed bed-mounted spheres) on the flow field. They argued that both sweep events and collisions are key factors in initiating the bedload motion. Most previous simulations on bedload transport over rough beds have been afflicted by simplification and idealized conditions, such as uniform spheres used as roughness elements. With the goal to study the flow and turbulence over natural bed roughness, several DNS-based research was conducted (e.g., Forooghi et al., 2018; Yuan & Piomelli, 2014). The exact details of a rough bed of a natural stream are generally not known; however, the bed roughness elevations follow a normal distribution (Nikora et al., 2001), which was incorporated in the LES roughness closure method proposed by Stoesser (2010).

In terms of statistical analysis of bedload parameters, a number of studies have analyzed the mean and standard deviation values of the dimensionless saltation length L_p, saltation height H_p, particle velocity U_p, particle angular velocity O_p, resting time T_r, and other parameters for different bed shear stresses (Bialik, 2011; Lee et al., 2000; Liu et al., 2019; Niño & García, 1998). Based on these parameters, the bedload transport rate q_b (in volume per unit width and time) is calculated as a product of the volumetric bedload concentration C_b, saltation height, and particle velocity, where C_b represents the volumetric proportion of saltating particles in the bedload layer. The particle spatial density φ, which is defined as the ratio of total projection area of particles onto the bed to the bed area, is a free parameter for erodible beds and has an impact on bedload transport. Additionally, statistical analysis (probability density distributions) of the parameters related to saltating particles has been carried out, but the findings from different studies are inconsistent. Roseberry et al. (2012) and Shim and Duan (2017) concluded that the saltation length obeys a gamma distribution, whereas the streamwise and spanwise particle velocities follow exponential and normal distributions, respectively. In contrast, Fathel et al. (2015) found that the saltation length follows a Weibull distribution, and the streamwise and spanwise particle velocities both follow exponential distributions. In addition, Hill et al. (2010) argued that the traversing length of particles follows an exponential distribution. Wu et al. (2020) argued that the predominance of mostly long hop particles results in a Gaussian-like velocity distribution, while a mixture of both short and long hop distance particles leads to an exponential-like velocity distribution. These discrepancies can be attributed to various conditions related to the flow, bedload particles, and boundary conditions. As a consequence, changes in the saltating particle statistics are affected by the bed roughness and particle spatial density. Other parameters, such as the angular velocity and resting time of particles, even though have been investigated by some previous studies, the PDF distribution of which have so far received inadequate studies. They are analyzed here.

In order to shed light on the effects of the natural bed roughness on bedload transport, this study focuses on two factors: the roughness height and particle spatial density. How these factors affect the flow and saltating particle characteristics in the case of an unsaturated bedload over a fixed bed is investigated. A roughness closure method is employed to generate a quasi-natural bed roughness. The Eulerian and Lagrangian point-particle methods are applied with the aid of LES to simulate the instantaneous fluid and bedload dynamics, respectively. The study focuses on the saltating mode, regarded as the dominant mechanism of bedload transport when the shear velocity is less than the settling velocity of the particles (Einstein, 1941; van Rijn, 1984). The experimental data of Niño and García (1998) are used as a reference case to validate the simulations. Keeping the same flow conditions, 12 cases using three bed roughness values (median bed particle diameters d_{50} = 0, 0.5, and 1.95 mm) and four particle spatial densities (φ = 0, 0.013, 0.104, and 0.312) are simulated. The flow regimes corresponding to the different roughness sizes range from hydraulically smooth flow to hydraulically rough flow. The hydrodynamics and particle saltation characteristics are analyzed and the bedload transport rate is estimated.

The remainder of this paper is structured as follows. The numerical framework is explained in Section 2. The numerical setup and boundary conditions are described in Section 3. The LES results are represented in Section 4. Finally, the discussion is provided in Section 5 and the conclusions are drawn in Section 6.

2. Numerical Framework

2.1. LES of Turbulent Flow

In this study, the Hydro3D LES code is employed to simulate the turbulent flow in an open channel. This code has been validated for many complex flows (Bai et al., 2013; Chua et al., 2019; Fraga & Stoesser, 2016; Liu et al., 2017; Ouro & Stoesser, 2019; Stoesser et al., 2015; Zhao et al., 2020). Stoesser et al. (2015) and McSherry et al. (2018) verified that the model can reproduce well the turbulence statistics of open-channel flow over rough walls and Zhao et al. (2020) verified that the saltating parameters of particles can be predicted well by the point-particle model.

The finite difference method is used on a staggered Cartesian grid to solve the filtered Navier-Stokes equations in Hydro3D, which is suitable for unsteady, incompressible, and viscous flow. The equations, which represent the conservation of fluid mass and momentum, are as follows:

$$\frac{\partial u_i}{\partial x_i} = 0, \tag{1}$$

$$\frac{\partial u_i}{\partial t} + \frac{\partial u_i u_j}{\partial x_j} = -\frac{1}{\rho}\frac{\partial p}{\partial x_i} + \frac{\partial (2\upsilon S_{ij})}{\partial x_j} - \frac{\partial \tau_{ij}}{\partial x_j} + f_{p,i} + f_{u,i}, \tag{2}$$

where u_i and u_j are the flow velocities in the i-direction and j-direction, respectively, and i and j correspond to numbers 1, 2, and 3 representing the x-direction, y-direction, and z-direction, respectively. At the same time, x_i and x_j are the spatial variables in the i-direction and j-direction, respectively, p is the instantaneous static pressure, ρ is the mass density of the fluid, ν is the fluid kinematic viscosity, and $f_{p,i}$ is the total force per unit volume exerted by the particles in the flow. $f_{p,i}$ can be obtained by $-m_p\,\Delta u_{p,i} / \Delta t\,\Delta V$, of which m_p is the total mass of the particle, including added mass, $\Delta u_{p,i}$ is the velocity increment during a unit interval Δt, ΔV is the unit volume of the grid. The particle's mass, m_p, can be calculated as $(\rho_s + C_m\,\rho)\pi d^3/6$, where ρ_s is the particle's density, C_m is the added mass coefficient, considered to be 0.5, and d_p is the nominal particle diameter. Then, interpolation functions, δ, are employed, based on distances between the particle and cells, to calculate the contribution of the force to fluid momentum and vice versa. The interpolation functions δ are introduced in the following section. $f_{u,i}$ is the forcing term from the roughness, which equals to $C - D + \nabla P + \Delta V/[\Delta t(U_{i,t} - U_i^n)]$ inside the roughness and 0 elsewhere, among which C is the discrete convection term, D is the discrete diffusion term, P is the resolved pressure divided by the density, V is the volume of the water, t is the time, U_i^n is the resolved velocity in i-direction at the previous time step and $U_{i,t}$ is the target velocity (here $U_{i,t} = 0$). The S_{ij} represents the strain-rate tensor, given by $(\partial u_i/\partial x_j + \partial u_j/\partial x_i)/2$, and τ_{ij} is the subgrid stress (SGS) tensor, defined as $\tau_{ij} = 2\nu_t S_{ij}$. Hence, it is the pressure gradient, which drives the channel flow in the simulation. In this study, the wall-adapted local eddy viscosity (WALE) model is adopted. Details of the WALE model can be found in Nicoud and Ducros (1999). Second-order and fourth-order central differences schemes are used to calculate the convective and diffusive velocity terms. A fractional step method is utilized for the time advancement, considered to be a predictor-corrector scheme. At every time step, a three-step Runge-Kutta scheme is applied to predict a nondivergence-free flow field which is then corrected by solving the Poisson pressure equation using a multigrid procedure. Velocities and pressure field are then updated accordingly. More details of the code are found in Cevheri et al. (2016) and Ouro et al. (2019).

2.2. Roughness Closure Method to Mimic a Natural Bed

The roughness closure method proposed by Stoesser (2010) is adopted here. In this method, the bed roughness height follows a normal distribution in compliance with sediment samples from natural and alluvial streambeds. Here, d_{50} is the median particle diameter and σ_b is the standard deviation of bed elevations, $0.5d_{50}$. A schematic view of the (artificially roughened) bed is shown in Figure 1a and a yz cross-section of three bed roughness heights Z_b are plotted in Figures 1b–1d. Among them, the ratio of the y scale to the z scale is 1:10. The median particle diameter d_{50} of the fixed bed increases from 0 to 1.95 mm, and as a consequence, the bed surface

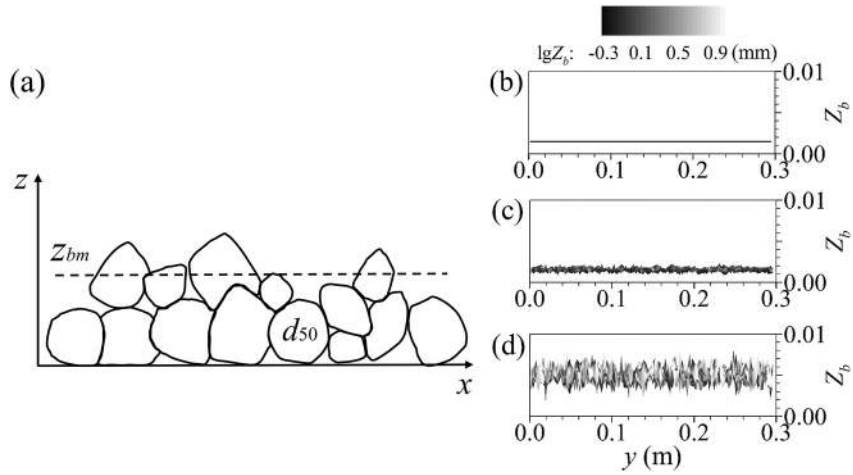

Figure 1. Rough bed as generated by employing the roughness closure method: (a) schematic view, and *yz* cross-section of bed roughness heights Z_b, S0 case (b), r0 case (c), and R0 case (d).

fluctuation increases from Figures 1b–1d. The characteristic parameters of a rough bed, e.g., mean value (Z_{bm}), maximum and minimum values (Z_{bmax} and Z_{bmin}) of bed surface fluctuations can easily be determined from the created bed. They are described in detail in Section 3. Hence, a more natural morphology of a fixed bed can be produced. It needs to be mentioned that the bedload transport study based on the fixed bed is different from erodible beds. In previous studies, significant local transport fluxes occur even at elevations deep within the bed under intense flow conditions (Berzi & Fraccarollo, 2016; Maurin et al., 2018; Pähtz & Durán, 2020). However, our study investigates relatively weak transport conditions for which the bed shear stress is slightly above the particle's critical shear stress.

2.3. Lagrangian Model of Particle Saltation

In order, to simulate the kinematics of a saltating particle, the Lagrangian point-particle model is applied to compute the particle's trajectory. In this model, the mobile particles are considered to be spherical and of the same size. Hence, Newton's second law and the Euler equations govern the particle translational and rotational motions as follows:

$$m_p \frac{du_{p,i}}{dt} = F_{p,i}, \tag{3}$$

$$I_p \frac{d\omega_{p,i}}{dt} = N_{p,i}, \tag{4}$$

where $u_{p,i}$ is the particle velocity in the *i*-direction and $F_{p,i}$ is the total force acting on the particle in the *i*-direction. For the rotational equation, $\omega_{p,i}$ is the particle angular velocity in the *i*-direction, I_p is the moment of inertia of the particle ($=m_p d^2/10$), and $N_{p,i}$ is the torque about the *i*-axis, which can be calculated from the following equation:

$$N_{p,i} = \frac{1}{2} C_\omega \rho |\omega_i - \omega_{p,i}| (\omega_i - \omega_{p,i}) \left(\frac{d_p}{2}\right)^5, \tag{5}$$

where ω_i is the fluid angular velocity around the particle about the *i*-axis and C_ω is the drag torque coefficient, a function of the rotational Reynolds number Re_ω ($=|\omega_i - \omega_{p,i}|(d_p{}^2/4)/\nu$) (Sawatzki, 1970). As the dominant particle rotational motion is around the *y*-axis, only rotation about the *y*-axis is considered in this study. Even though the mobile bedload particles are also nonspherical and follow a normal distribution in a natural stream, such complexities are ignored in the present study, which may lead to simplification for calculation of their forces as well as collision process.

The total force acting on a particle is rather complicated, involving the particle submerged weight $F_{G,3}$, hydrodynamic drag $F_{D,i}$ and lift $F_{L,i}$, bed friction $F_{f,i}$, and the Basset force $F_{B,i}$. These forces are determined as follows.

The submerged weight of a particle is expressed as

$$F_{G,3} = \frac{1}{6}(\rho_s - \rho)\pi g d_p^3, \tag{6}$$

where g is the gravitational acceleration, equaling 9.81 m/s^2.

The hydrodynamic drag caused by viscous skin friction and the pressure differences due to the particle-fluid slip velocity is given by

$$F_{D,i} = \frac{1}{2}C_D \rho A_f |u_i - u_{p,i}|(u_i - u_{p,i}), \tag{7}$$

where A_f is the area of the particle projected on a plane normal to the flow direction, u_i is the flow velocity in the i-direction, and C_D is the drag coefficient. For spherical particles, various equations for C_D have been derived (Brown & Lawler, 2003; Lukerchenko et al., 2012; Schiller & Naumann, 1935; Stokes, 1851; Swamee & Ojha, 1991). In the present study, the equation of Brown and Lawler (2003) is used here

$$C_D = \frac{24}{Re_p}\left(1 + 0.15Re_p^{0.681}\right) + 0.407\left(1 + \frac{8710}{Re_p}\right)^{-1}, \left(Re_p \le 2 \times 10^5\right), \tag{8}$$

where Re_p is the particle Reynolds number, given by $Re_p = u_i - u_{p,i}d_p/\nu$. It is found that the calculated Re_p and the magnitude of difference between fluid and particle velocity near the bed are 16.42 and 0.032 m/s.

Delta functions, δ, are employed to interpolate the local flow velocity field to the centroid of the particle, from which particle forces are subsequently computed. The delta functions δ are calculated as a result of three one-dimensional kernels ϕ as

$$\delta\left(\frac{\boldsymbol{x} - \boldsymbol{x}_p}{\Delta \boldsymbol{x}}\right) = \frac{1}{\Delta x_i}\phi\left(\frac{x_i - x_{p,i}}{\Delta x_i}\right)\phi\left(\frac{x_j - x_{p,j}}{\Delta x_j}\right)\phi\left(\frac{x_k - x_{p,k}}{\Delta x_k}\right), \tag{9}$$

where $\boldsymbol{x}$ and $\boldsymbol{x}_p$ are coordinates of the Eulerian cell and Lagrangian particles, respectively. $\Delta \boldsymbol{x}$ is the volume of an Eulerian cell given by $\Delta xi \Delta xj \Delta x_k$. The normalized grid spacing n equals $(\boldsymbol{x} - \boldsymbol{x}_p)/\Delta \boldsymbol{x}$ and the kernel functions ϕ_3 of Roma et al. (1999) are applied as

$$\phi_3(n) = \begin{cases} \frac{1}{3}\left(1 + \sqrt{-3n^2 + 1}\right) & \text{if} |n| < 0.5 \\ \frac{1}{6}\left(5 - 3|n| - \sqrt{-3(1 - |n|)^2 + 1}\right) & \text{if} 0.5 \le |n| < 1.5 \\ 0 & \text{if} |n| \ge 1.5 \end{cases}, \tag{10}$$

This means that flow information of three neighboring fluid cells in each direction are utilized to relate the fluid force to the particle and vice versa.

The total lift $F_{L,i}$ is the sum of the Saffman lift $F_{Saff,i}$ and the Magnus lift $F_{Mag,i}$. The former results from the nonuniform pressure distribution induced by the velocity gradient, whereas the latter is due to particle rotation. The expressions for the total lift, Saffman lift, and Magnus lift are as follows:

$$F_{L,i} = F_{Saff,i} + F_{Mag,i}, \tag{11}$$

$$F_{Saff,i} = \frac{1}{2}C_L \rho A_f \left(u_{rT,i}^2 - u_{rB,i}^2\right), \tag{12}$$

$$F_{Mag,i} = \frac{1}{8}\rho \pi d_p^3 \omega_{p,i} |u_i - u_{p,i}|, \tag{13}$$

where $u_{rT,i}$ and $u_{rB,i}$ are the slip velocities at the top and bottom of a particle, respectively, and C_L is the lift coefficient. The values of C_L are various for different researchers (Barati et al., 2018; Krecic & Hanes, 1996; Lee & Balachandar, 2017; Lee & Hsu, 1994; Lee et al., 2000, 2006; Lukerchenko et al., 2012; Wiberg & Smith, 1985).

More information on C_L are available in Dey et al. (2020). Since there is no consensus for the values of C_L, the C_L is treated to be a constant as 0.4 in this study, according to the experimental result of Niño and García (1998).

When the upward forces acting on the particle could not offset its submerged weight, it eventually returns to the bed, where it decelerates until it stops. At this instant, the friction force can be calculated as follows:

$$F_f \le \mu F_n, \tag{14}$$

where μ is the dynamic friction coefficient, whose value is roughly equal to the tangent of the local pivoting angle of the local bed profile by Wiberg and Smith (1987). In this code, in order to simplify the calculation, it is treated as a constant of 0.6. F_n is the total normal reaction force from the bed acting on the particle, which equals the difference between the downward particle submerged weight and other upward forces. Similarly, if the dynamic forces acting on the particle are larger than its submerged weight or static friction force, particle motion is initiated upward or forward.

The Basset force, which is also called the history force, is caused by the temporal delay from the boundary layer surrounding the particle in the process of acceleration and deceleration (Crowe et al., 1998). The expression for the Basset force is as follows:

$$F_{B,i} = \frac{3}{2} d_p^2 \sqrt{\pi \upsilon} \int_0^t \frac{\frac{du_i}{d\eta} - \frac{du_{p,i}}{d\eta}}{\sqrt{t-\eta}} d\eta, \tag{15}$$

where t is the dimensionless time and η is the dummy variable for integration. Because the accurate prediction of the Basset force depends on the accuracy of Basset kernels, it has been found harder to be predicted. Even in the simple case of unidirectional acceleration of a particle in an unbounded quiescent fluid, the Basset kernel can be very complex (Lee et al., 2011). However, this force is more important for sand particles than for gravels (Bombardelli et al., 2008), so that it cannot be ignored here.

There are three methods of solving the Basset kernels (the integral term): the semi-derivative approach of Bombardelli et al. (2008) and the trapezoidal-based methods of van Hinsberg et al. (2011) and Daitche (2013). In this study, the semi-derivative approach is employed, which can be described as follows:

$$\int_a^t \frac{\frac{du_i}{d\eta} - \frac{du_{p,i}}{d\eta}}{\sqrt{t-\eta}} d\eta = \int_a^t \frac{1}{\sqrt{t-\eta}} \frac{du_r}{d\eta} d\eta = \Gamma(0.5) \frac{d^{-0.5} \frac{du_r}{d\eta}}{[d(t-a)]^{-0.5}}, \tag{16}$$

where $\Gamma(x)$ is the gamma function. For a general function f, the semi-derivative can be calculated as

$$\frac{d^{-0.5} f}{[d(t-a)]^{-0.5}} = \lim_{N \to \infty} \left[\left(\frac{t-a}{N} \right)^{0.5} \frac{1}{\Gamma(0.5)} \sum_{k=0}^{N-1} \frac{\Gamma(k+0.5)}{\Gamma(k+1)} f \left[t - \frac{k(t-a)}{N} \right] \right], \tag{17}$$

where N is the number of terms considered in the semi-derivative summary, k is the dummy variable (=0 to $N-1$), and a is the lower limit of integration, set to 0 for the classical definition of the Basset force. To calculate the term including the gamma function, the approximate equation $\Gamma(x) = \sqrt{2\pi}\ \exp(-x) x^{x-0.5}$ can be used. This can be solved as follows:

$$\frac{\Gamma(k+0.5)}{\Gamma(k+1)} = \exp[0.5 + k \ln(k+0.5) - (k+0.5)\ln(k+1)]. \tag{18}$$

Additionally, the memory time period must be considered in calculating the Basset force. Here, the method proposed by Bombardelli et al. (2008) is used, which adopts the largest value among the particle relaxation time $\rho_s d_p^2/(18\rho\nu)$, the flow characteristic time $80\nu/u_*^2$, and the Basset force scaling time $2\nu/u_*^2$. However, Bombardelli et al. (2008) overlooked the Basset force contribution during particle-bed collisions in that the computation of the Basset force was set to zero after each rebound against the wall (Lukerchenko, 2010; Lukerchenko et al., 2012). In the present model, the velocity change after the collision is recorded for calculating the Basset force.

2.4. Collision Model

Collision is an important aspect of the saltating motion of particles in the bedload. The energy loss resulting from the sphere-wall collisions in a glycerin-water mixture were studied experimentally by McLaughlin (1968). Relatively complex experiments, such as oblique particle-wall collisions and three-sphere collisions, were later conducted (Donahue et al., 2010; Joseph & Hunt, 2004). On the basis of experimental results, several collision models were developed, and widespread attention has focused on the numerical modeling of the collision processes. One of the common methods is to utilize two coefficients, e.g., friction coefficient f_0 and restitution coefficient e, in a collision-rebound model and to compute the gravel velocities after collisions. The coefficient values used in collision models by different researchers are various (Bialik, 2011; Gordon et al., 1972; Kharlamova & Vlasák, 2015; Maldonado & Borthwick, 2014; Schmeeckle et al., 2001; Wiberg & Smith, 1985). It has been found that the tangential component usually dominates in particle-bed collisions while the restitution coefficient e has a very minor effect (Pähtz et al., 2020). In the case of a particle-resolved DNS, the entire collision process can be calculated by decomposing the system into several phases, so that the lubrication force within the gap between the colliding particles is also included (Kempe & Fröhlich, 2012).

In this study, as proposed by Niño and García (1998), the particle-wall collision model is used with a friction coefficient of $f_0 = 0.89$ and a restitution coefficient of $e = 0.75-0.25(\tau_*/\tau_{*_c})$. That is,

$$u_{t,out} = f_0 u_{t,in}, \tag{19}$$

$$u_{n,out} = -e u_{n,in}, \tag{20}$$

where $u_{t,in}$, $u_{t,out}$, $u_{n,in}$, and $u_{n,out}$ represent the tangential and normal velocity of the particle based on the coordinates according to the collision surface before and after the collision, respectively. They can be transferred to velocities in the Eulerian coordinate system. More details can be found in Niño and García (1998). Because the positions of the center of the particles have been tracked during the simulation, once it is found that the distances between them and the rough bed below them are less than their radius, particle-wall collision occurs. The particle-particle collisions maybe solved by the model of Glowinski et al. (1999) by activating a repulsive force when particles are close to each other with the goal to prevent particle overlapping. However, this is forgone herein because of the relatively low particle spatial density, assuming that particle overlaps occurs very rarely.

3. Numerical Setup and Boundary Conditions

The simulations are conducted on the Hawk supercomputer at Cardiff University, UK. By using 128 processors, a rectangular open channel of size $L_d \times B \times h = 0.8\ \text{m} \times 0.3\ \text{m} \times 0.035\ \text{m}$ is simulated, matching exactly the conditions of experiment S12 of Niño and García (1998). A schematic of the simulation domain is shown in Figure 2a including sediment particles (in blue), whose size is enlarged to visualize their starting locations. The parameters used in experiment S12 are provided in Table 1. The simulation domain consists of $1536 \times 100 \times 40$ grid points. Mobile particles, classified as sand, with $d_p = 0.5$ mm and $\rho_s = 2650\ \text{kg/m}^3$ are randomly placed on the bed within the domain with zero particle velocity. Table 2 summarizes the 12 simulations performed using combinations of three bed conditions and four particle spatial densities. All sidewalls are assumed to be smooth. The characteristics of the rough bed are given in Table 3 and the three bed geometries are presented in Figures 2b–2d.

In order to mimic an infinitely long open-channel flow and to allow direct comparisons with the experiment from Niño and García (1998), periodic boundary conditions are applied to the streamwise direction of both the flow and the bed particles. The no-slip condition is applied to the spanwise direction and at the channel bed. The free surface is considered as a rigid lid, with the free-slip condition justified by the relatively flat free surface and low Froude numbers of the simulated flows.

A variable time step is used based on maximum CFL = 0.35. The ratio of domain length to mean flow velocity is defined as the flow through (FT) time and the ratio of flow depth to shear velocity is defined as the eddy turnover (ET) time. As a precursor simulation, the model is executed for 65 FTs or 131 ETs without particles to establish fully developed turbulent flow. Another 98 FTs or 199 ETs are then simulated including the particles to collect flow and particle statistics.

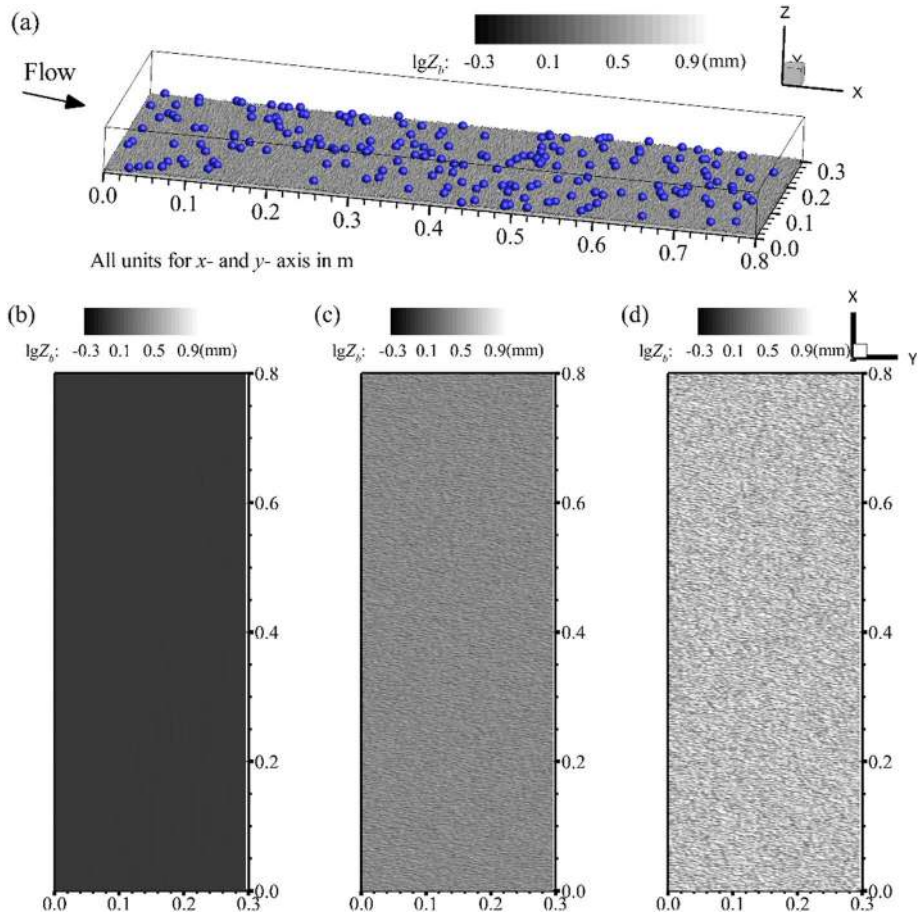

Figure 2. Schematic of the simulation domain including the initial placement of the particles (a), visualization of the rough beds, S0 case (b), r0 case (c), and R0 case (d).

4. Results

4.1. Hydrodynamics

In order to calculate bed shear stress F_b, the friction due to side walls F_w should be removed from the total shear stress F_{tot}, that is $F_b = F_{tot} - F_w$. Among them, F_{tot} can be obtained as $\rho L_d \times dp/dx \times h \times B$ and F_w can be obtained as $2\rho\upsilon \times du/dy \times h \times L_d$, of which dp/dx is the dimensionless time-averaged pressure gradient and du/dy is the averaged velocity gradient along the spanwise direction. As the bed shear stress F_b can be derived from $\rho u_*^2 \times L_d \times B$, the shear velocity u_* can finally be determined as $(dp/dx \times h - 2\upsilon \times du/dy \times h/B)^{0.5}$. The friction Reynolds number Re_τ is given by $u_* h/\nu$. The dimensionless grid spacing in the horizontal and vertical directions in terms of wall units can be expressed as Δx^+, $\Delta z^+ = (\Delta x, \Delta z/2) \times (u_*/\nu)$, respectively. Information about the grid resolution are summarized in Table 4.

Table 1
Parameters in Experiment S12 of Niño and García (1998)

Parameter	Niño and García (1998)
Median particle diameter d_{50} (mm)	0.5
Channel width B (m)	0.3
Flow depth h (mm)	35
Mean flow velocity u_0 (m/s)	0.316
Shear velocity u_* (m/s)	0.024
Reynolds number $Re = u_0 h/\nu$ (−)	10955
Froude number $Fr = u_0/(gh)^{0.5}$ (−)	0.541

In Table 4, the computed friction Reynolds number and the shear velocity increase, as the value of bed roughness increases. In order to balance between capturing the turbulent vortex structures near bed and achieving the validity of the Lagrangian Particle Tracking, the grid resolution in the x-direction and z-direction are chosen as above table shows. As Δx^+ is 14.5–27.5 and Δz^+ is 8.0–15.3, the size of the grid spacing is adequate to resolve the large scales of turbulence (Rodi et al., 2013). In addition, as the simulated shear velocities are obtained, the flow characteristics over smooth and rough beds can be determined. In case of a flume without mobile bed particles, the flow characteristics for the three bed conditions are provided in Table 5, where k_s^+

Table 2
Simulation Cases

Particle spatial density φ	0%	0.013	0.104	0.312
Smooth bed (d_{50} = 0 mm)	S0	S1	S2	S3
Rough bed 1 (d_{50} = 0.5 mm)	r0	r1	r2	r3
Rough bed 2 (d_{50} = 1.95 mm)	R0	R1	R2	R3

represents the roughness Reynolds number, given by $k_s u_*/\nu$, which determines the flow regime (for hydraulically smooth flow $k_s^+ \leq 5$, for hydraulically transitional flow $5 < k_s^+ < 70$, and for hydraulically rough flow $k_s^+ \geq 70$). Thus, cases S0, r0, and R0 represent hydraulically smooth, transitional, and rough flow, respectively.

The velocity spectral density function in an open-channel flow consists of at least three ranges (Nikora, 2005). The largest eddies are found within the energy-containing range (0 slope), successively smaller eddies in the inertial subrange (−5/3 slope), are governed by the Taylor microscale, and the smallest eddies are found in the dissipation range (steeper slope), governed by the Kolmogorov scale. Based on a simulation velocity time series, the velocity spectral density function S versus frequency f is plotted in Figure 3. The spectrum represents the velocity series in the frequency domain at the midflow depth in the computational domain. The three ranges are evident in Figure 3. The −5/3 slope spans slightly more than a decade of frequencies, which is sufficient for an LES given the relatively high flow Reynolds number. The slope then steepens because the SGS model introduces energy dissipation at a high rate.

With the aim to investigate the turbulent flow characteristics, contours of the dimensionless streamwise-averaged streamwise velocity $\langle u\rangle^+$ and Reynolds shear stress $-\langle\overline{u'w'}\rangle/u_*^2$ under the three bed conditions are plotted on the yz-plane (across the flow) in Figures 4a–4c and 4d–4f, respectively. Here, $\langle u\rangle^+$ is defined as $\langle u\rangle/u_*$, where u is the time-averaged streamwise velocity, u' and w' are the fluctuations of instantaneous streamwise and vertical velocity components with respect to their time-averaged values, respectively, and $\langle\cdot\rangle$ denotes the spatial averaging of a quantity over the streamwise length of the domain. The dimensionless vertical scale is z'/h', where $z' = z - Z_{bm}$ and $h' = h - Z_{bm}$. The velocity distribution at the corner of the cross-section reflects secondary currents caused by the sidewalls. These are particularly significant for the S0 and r0 cases ($k_s^+ = 0$ and 15, respectively), but the secondary currents are weaker for the R0 case ($k_s^+ = 128$). This is illustrated with vectors of the streamwise-averaged secondary velocity plotted in Figures 5a–5c. Circulation in the bottom two corners is indeed significant for the S0 case and decreases, as the roughness increases. This suggests that stronger turbulence due to bed roughness disrupts the secondary flow and leads to a relatively uniform flow field. The Reynolds shear stress attains a peak much closer to the bed in the smooth bed case (S0 case, $k_s^+ = 0$) than in the rough-bed cases. As the bed roughness increases, the maximum value of the Reynolds shear stress decreases, because the pressure drag plays an increasingly important role, as the bed becomes rougher.

Profiles of the dimensionless streamwise-averaged and time-averaged streamwise velocity $\langle u\rangle^+$, Reynolds shear $-\langle\overline{u'w'}\rangle/u_*^2$, and normal stresses $\langle\overline{u_i'u_i'}\rangle/u_*^2$ at $y = B/2$ are plotted in Figures 6a–6c. Figure 6a presents $\langle u\rangle^+$ as a function of dimensionless vertical distance z^+ in a semi-logarithmic plot. The vertical distance z is scaled with the viscous units as $z^+ = zu_*/\upsilon$ for smooth bed ($k_s^+ = 0$), and scaled with the roughness height as $z^+ = z/k_s$ for rough bed ($k_s^+ = 15, 128$). As the bed roughness k_s increases, the z/k_s decreases and two rough-bed $\langle u\rangle^+$ profiles exhibit a clear leftward shift from the smooth bed profile (black line), the latter exhibiting a clear logarithmic behavior above the viscous sublayer and the buffer layer (i.e., for $z^+ > 40$). These findings are in agreement with the previous simulations and experimental observations (Nikora, 2005; Rahman & Webster, 2005), in which the velocity profile in a smooth bed has a similar trend. The two rough-bed velocity profiles feature a linear part in the roughness layer and a logarithmic part. The slope of the profiles of the logarithmic part is same as that of the smooth bed profile, relating to the derivative of von Kármán constant. The $-\langle\overline{u'w'}\rangle/u_*^2$ profiles for the three beds are similar (Figure 6b), each attaining peak values near the bed and exhibiting a linear decrease toward the free surface. This finding corresponds to those of previous studies (Chan-Braun et al., 2011; Mazzuoli &

Table 3
Characteristics of Two Rough Beds

Parameter	Rough bed 1 (d_{50} = 0.5 mm)	Rough bed 2 (d_{50} = 1.95 mm)
Mean value of bed elevation Z_{bm} (mm)	1.555	4.925
Maximum value of bed elevation Z_{bmax} (mm)	2.682	9.102
Minimum value of bed elevation Z_{bmin} (mm)	0.434	0.434

Table 4
Grid Resolution Summary

Case	Dimensionless time-averaged pressure gradient dp/dx (−)	Friction Reynolds number $Re_\tau = u_* h/\nu$ (−)	Aspect ratio h/B (−)	Simulated shear velocity u_* (m/s)	Grid spacing Δx, Δz (mm)	Dimensionless grid spacing Δx^+, Δz^+ (−)
S0	0.01224	643.5	0.116	0.01854	0.78125, 0.8675	14.5, 8.0
S1	0.01223	643.1	0.116	0.01853	0.78125, 0.8675	14.5, 8.0
S2	0.01222	642.8	0.116	0.01853	0.78125, 0.8675	14.5, 8.0
S3	0.01240	647.5	0.116	0.01866	0.78125, 0.8675	14.6, 8.1
r0	0.01499	734.6	0.116	0.02222	0.78125, 0.8675	17.3, 9.6
r1	0.01499	739.5	0.116	0.02227	0.78125, 0.8675	17.4, 9.6
r2	0.01307	688.3	0.116	0.02077	0.78125, 0.8675	16.2, 9.0
r3	0.01324	691.8	0.116	0.02087	0.78125, 0.8675	16.3, 9.0
R0	0.04155	1048.7	0.116	0.03516	0.78125, 0.8675	27.4, 15.2
R1	0.04147	1047.6	0.116	0.03512	0.78125, 0.8675	27.4, 15.2
R2	0.04191	1050.7	0.116	0.03528	0.78125, 0.8675	27.5, 15.3
R3	0.04163	1047.2	0.116	0.03517	0.78125, 0.8675	27.4, 15.2

Uhlmann, 2017; Nezu & Nakagawa, 1993; Nikora, 2005). As k_s^+ increases, the vertical point at which the peak occurs increases from $z/h = 0.1$ to 0.16. The peaks of the dimensionless streamwise normal stress profiles, which are plotted in Figure 6c, decrease with an increase in roughness, while the profiles of the other two components are quite similar. However, the elevations at which the peaks occur increase from $z/h = 0.049$ to 0.13, as the bed roughness increases.

Contours of the dimensionless streamwise velocity fluctuations, scaled with the shear velocity u_*, on a xy-plane (horizontal plane) at a given vertical elevation are presented in Figures 7a–7c. In Figures 7a–7c, the xy-plane for the smooth bed ($k_s^+ = 0$) is located at $z = \delta$, where δ is the viscous sublayer thickness ($11.6\nu/u_*$), and the xy-plane for the rough bed ($k_s^+ > 0$) is at $z = d_{50}$. In Figure 7a, the coherent structures comprising high-speed and low-speed streaks are evident at an approximately regular spanwise spacing. Most of the turbulence production takes place due to elongated alternating patches of high-speed and low-speed fluid streaks, triggering streamwise vorticity and the near-bed bursting phenomenon, involving ejections and sweeps. This is a quasi-periodic process whereby the near-bed low-speed fluid entrains from the bed into the upper layers of the flow and high-speed fluid rushes from the upper layers flow toward the bed (Dey, 2014). Besides, it is also found that the near-bed sweep is responsible for initiating the instability of the sand bed (Khosronejad & Sotiropoulos, 2014, 2017; Khosronejad et al., 2020). Noteworthy is that the streaks gradually disappear with an increase in bed roughness, which disrupts the organization of the streaks (Figures 7b and 7c). This is due to the roughness elements protruding into the near-wall flow breaking up elongated streaks into irregular, smaller fragments.

Table 5
Flow Characteristics for Three Bed Conditions

Cases	d_{50} (mm)	u_* (m/s)	k_s (mm)	k_s^+ (−)	Flow regime
S0	0	0.01854	0	0	Smooth flow
r0	0.5	0.02222	0.66	15	Transitional flow
R0	1.95	0.03516	3.64	128	Rough flow

4.2. Particle Saltation Statistics

To conveniently compare the saltation parameters with the previous studies, regardless of the flow conditions and sediment particle sizes, the dimensionless saltation length L_p, saltation height H_p, particle velocity U_p, angular velocity O_p, and resting time T_r are defined as follows:

$$L_p = \frac{l_p}{d_p}, \tag{21}$$

$$H_p = \frac{h_p}{d_p}, \tag{22}$$

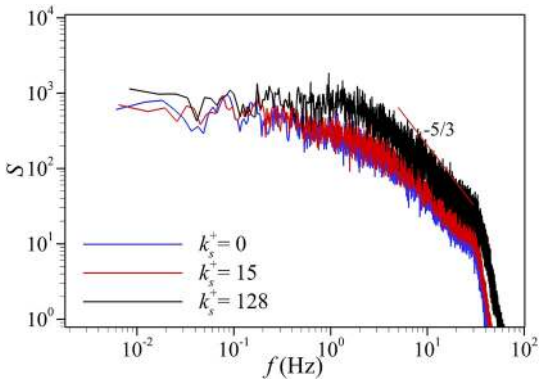

Figure 3. Velocity spectra for three bed conditions detected at the midflow depth in the computational domain.

$$U_p = \frac{u_p}{u_*}, \tag{23}$$

$$O_p = \frac{o_p d_p}{u_*}, \tag{24}$$

$$T_r = \frac{t_r u_*}{d_p}, \tag{25}$$

where d_p is the mobile particle diameter, l_p is the saltation length, h_p is the saltation height, u_p is the particle velocity, o_p is the particle angular velocity, and t_r is the resting time. It is worth emphasizing that all particles statistics mentioned here are collected above a rigid bed of which particles entrained by the flow move more quickly than over a mobile bed (Lajeunesse et al., 2010). Under this circumstance, the saltation length, analogous to the experimental results measured by Niño and García (1998), is defined as the total distance traveled by the particle between subsequent collisions with the bed, which differs from the measured "hop length," the distance from start to stop of particles, by some researchers (Fathel et al., 2015; Roseberry et al., 2012; Wu et al., 2020). The saltation height is the maximum height the particle attains and the particle's velocity and its angular velocity pertain to their time-averaged value during the saltation event between subsequent collisions with the bed. The resting time is defined as the time period from a particle to return to the bed until it bounces up again. The initiation and halting of particle motion are determined by the total dynamic forces acting on the particle. This information can be used to calculate the acceleration and then to derive the velocity of the particles from the known time step. When this predicted velocity is larger than 0 in an arbitrary direction, particle motion is initiated toward this direction. Besides, when the particle falls back to the bed and the predicted velocity is less than 0 in an arbitrary direction, the particle motion stops in this direction and becomes static if all velocities become 0.

The flow condition related to a specific particle size can be characterized by the stress ratio Θ/Θ_c, where Θ and Θ_c represent the Shields parameter and critical Shields parameter for bed particle motion, respectively. In order

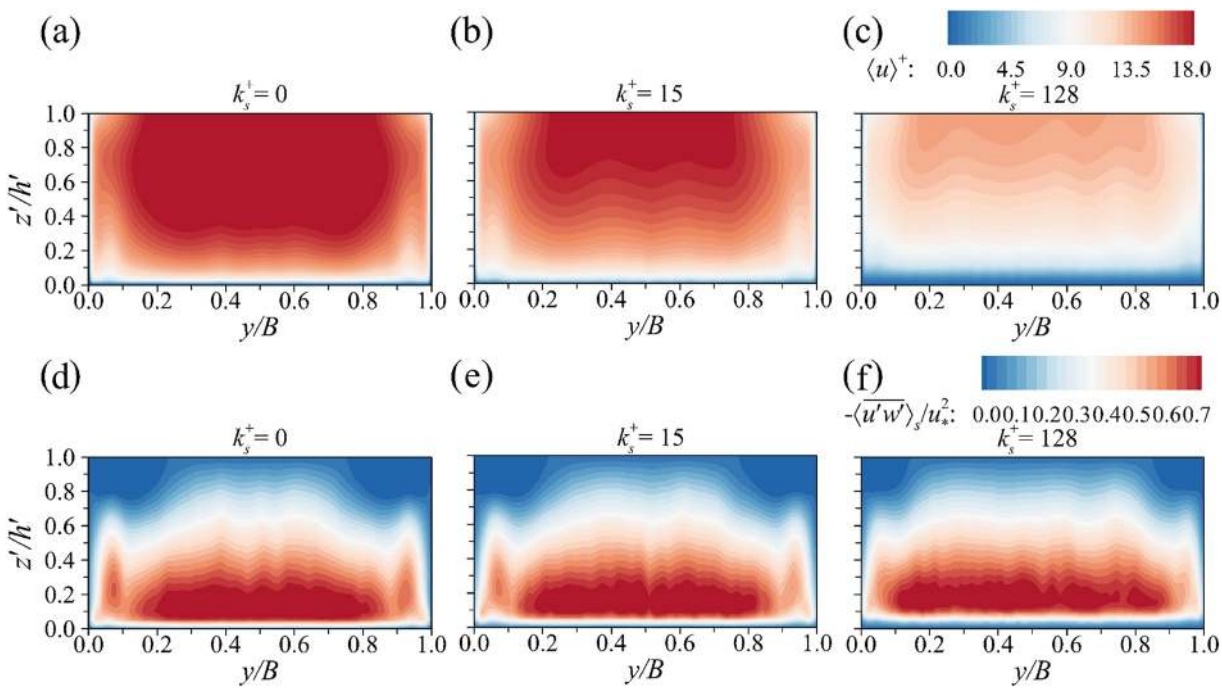

Figure 4. Contours of the streamwise-averaged streamwise velocity and Reynolds shear stress for cases: (a) and (d) S0 ($k_s^+ = 0$), (b) and (e) r0 ($k_s^+ = 15$), (c) and (f) R0 ($k_s^+ = 128$).

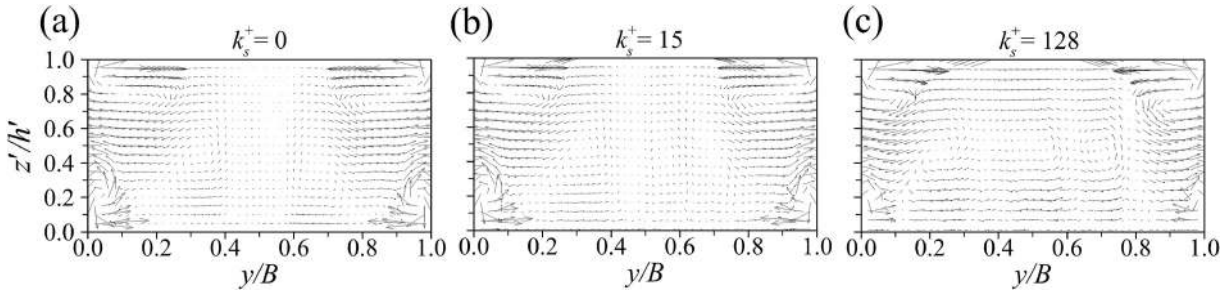

Figure 5. Vectors of the streamwise-averaged secondary velocity for cases: (a) S0 ($k_s^+ = 0$), (b) r0 ($k_s^+ = 15$), and (c) R0 ($k_s^+ = 128$).

to obtain the critical Shields parameter Θ_c, the critical shear velocity u_{*c} is determined from the Shields diagram (Vanoni, 1975), found to be 0.032 herein. The Shields parameter Θ can be calculated as

$$\Theta = \frac{u_*^2}{gRd_p}, \tag{26}$$

where R is the submerged relative density of particles, i.e., $(\rho_s - \rho)/\rho$.

It is pertinent to mention that in cases S0, r0, and R0, where in fact the beds contain 200 particles in the relatively large domain, the particle spatial densities, are deemed to be zero ($\varphi = 0$), i.e., negligible. As there are very few particles on the bed surface, it is assumed that particles do not interact. Hence, the statistical analysis is applied to the saltating particle characteristics in cases S0, r0, and R0 for specific flow conditions affected by the bed roughness, but the particle spatial density is not considered. Specifically, the samples for the statistical analysis are taken from 200 particles during the entire simulation. Case r0, in which both the bed particles and movable bed particles measuring 0.5 mm, is closest to the experimental condition of Niño and García (1998).

The standard deviation of the particle saltation length, saltation height, velocity, angular velocity, and resting time are plotted in Figures 8a–8e, together with data from experiment S12 of Niño and García (1998). Both the simulated mean values and the standard deviations agree with the experimental data, especially the standard deviations, which were found to be larger in previous simulations (Barati et al., 2018; Bialik, 2011). Especially, the values of dimensionless saltation length and height are around 10 and 1, when the stress ratio Θ/Θ_c ranges from 1 to 2, which is also consistent with the research of Abbott and Francis (1977). In terms of the dimensionless angular velocity, the simulation results also correspond well with the linear relationship proposed by Niño and García (1998). As the roughness Reynolds number k_s^+ increases, the stress ratio Θ/Θ_c increases, but the saltation length, particle velocity, and angular velocity decrease significantly. This trend contradicts the finding that the increase in Θ/Θ_c from the enhanced flow intensity leads to an increased or unaffected saltation length (Fraccarollo & Hassan, 2019). This can be attributed to the fact that the rough bed contains some pits that may trap particles. This can also be verified from the particles' resting times, which increase, as the bed becomes rougher. With regard to the saltation height, no significant change is found with respect to bed roughness.

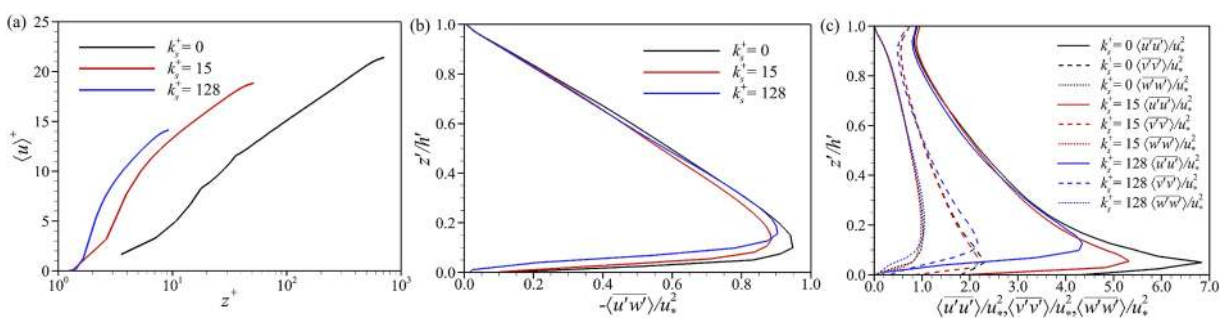

Figure 6. Vertical profiles of dimensionless streamwise-averaged and time-averaged flow parameters without mobile bed particles for the three beds at location $y = B/2$ ($k_s^+ = 0$, 15, and 128), (a) streamwise velocity $\langle u \rangle^+$, (b) Reynolds shear stress $-\langle \overline{u'w'} \rangle/u_*^2$, and (c) Reynold normal stresses $\langle \overline{u_i'u_i'} \rangle/u_*^2$.

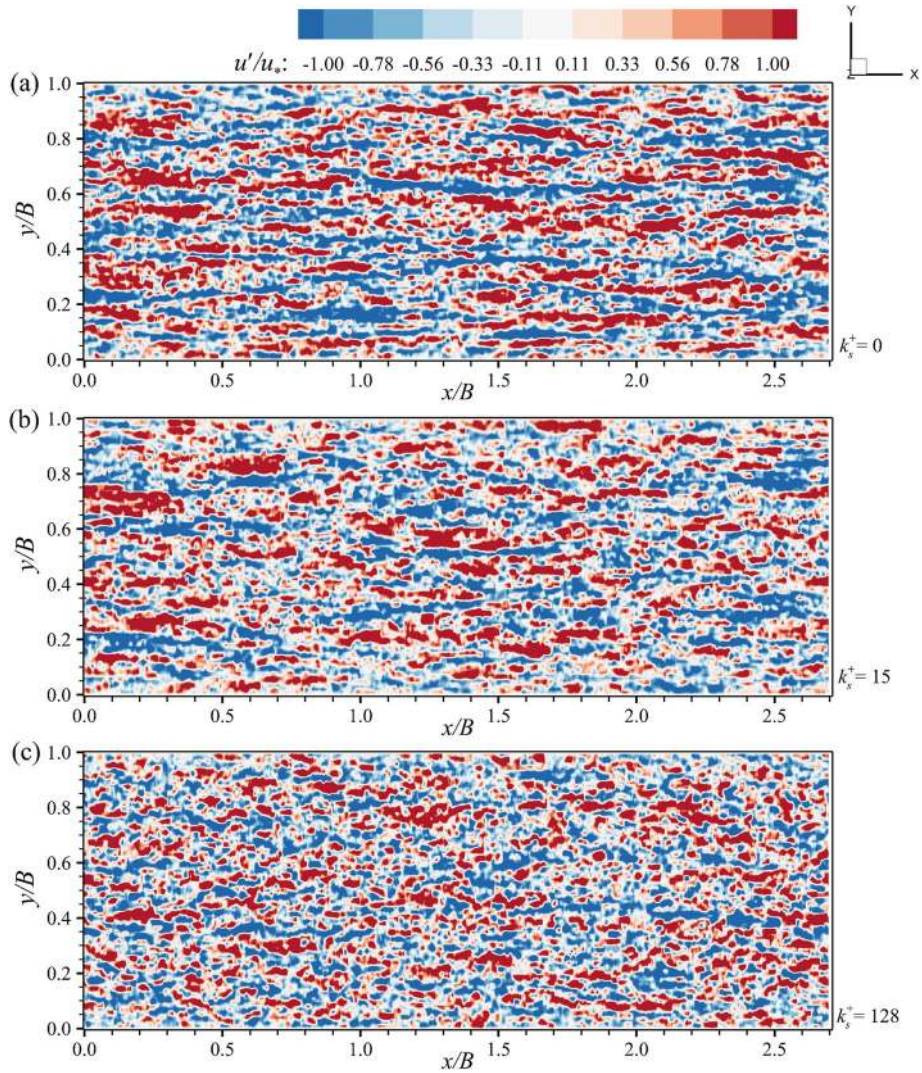

Figure 7. Contours of dimensionless streamwise velocity fluctuations u/u_* on xy-planes at $z = \delta$ for $k_s^+ = 0$ and $z = d_{50}$ for $k_s^+ > 0$. (a) S0 case ($k_s^+ = 0$), (b) r0 case ($k_s^+ = 15$), and (c) R0 case ($k_s^+ = 128$).

With the goal to investigate further the bedload saltation statistics for all cases with increased particle spatial density, all data obtained from randomly selected 1 000 particles during the nine simulations are listed in Table 6. No significant change is noticeable for any of the dimensionless parameters except for T_r. It is evident that T_r decreases, as the particle spatial density increases from 0.013 to 0.312, and the degree of reduction is even stronger for relatively rough beds (R1–R3). The reason is that the increase of particle spatial density results in an enhanced interaction between particles by flow affection, and so particles that lie in troughs in between roughness elements are disturbed and set in motion.

4.3. Distribution of Bedload Statistics

To extend the investigation to the distribution of key saltation parameters, the probability density function (PDF) distributions for the three conditions ($k_s^+ = 0$, 15, and 128) are plotted in Figures 9a–9e. Here, the primary concern is the change in the PDF distributions caused by the roughness. The statistics given by a particle spatial density $\varphi = 0.013$ are chosen as representative values, because the distribution of the key parameters (with the exception of the resting time) do not vary significantly, as the particle spatial density increases.

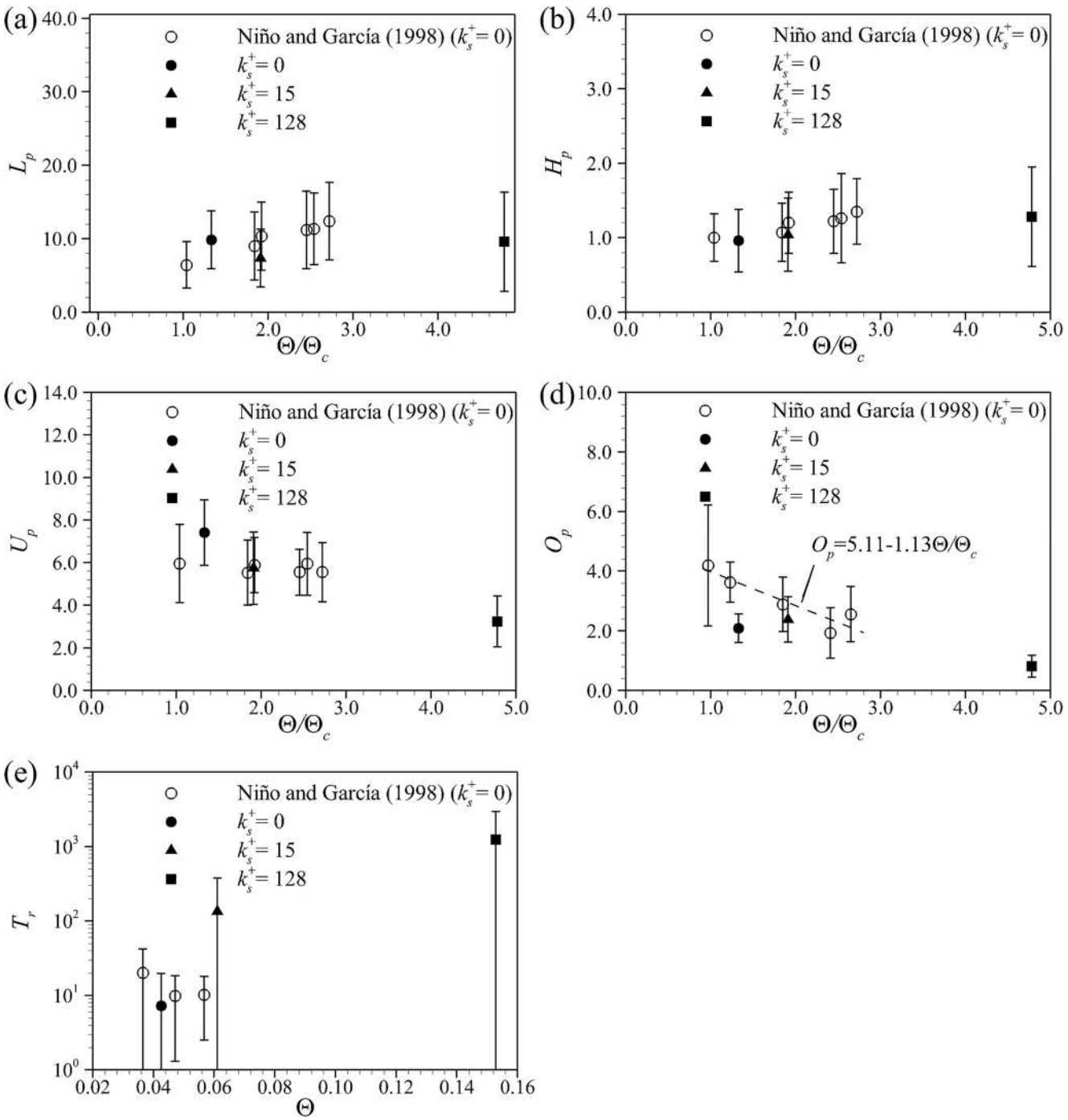

Figure 8. Computed dimensionless saltation parameters of bedload particles of the three beds (cases S0 ($k_s^+ = 0$), r0 ($k_s^+ = 15$), and R0 ($k_s^+ = 128$)) and experimental data of Niño and García (1998). (a) Saltation length L_p, (b) saltation height H_p, (c) particle velocity U_p, (d) angular velocity O_p, and (e) resting time T_r. Symbols represent the mean values, vertical lines represent the total length of two standard deviations, and the broken line represents the linear relationship fitted to mean values after Niño and García (1998).

A close observation of Figures 9a–9e shows significant changes for five parameters (H_p, L_p, U_p, O_p, and T_r). In order to quantify the description of PDF distributions, further analysis has been carried out to represent more details of those statistics and to support the results shown in Figure 9 as well. Coefficients of skewness (*SK*) and kurtosis (*KU*) for the smooth bed case ($k_s^+ = 0$) are calculated and shown in Table 7, in which skewness and

Table 6
Simulated Results of Bedload Saltation Statistics for Nine Cases Compared With the Experiment Results of Niño and García (1998)

Cases	L_p	rms L_p	H_p	rms H_p	U_p	rms U_p	O_p	rms O_p	T_r	rms T_r
Exp. S12	9.00	4.63	1.07	0.39	5.53	1.52	3.05	1.00	10.00	10.00
S1	9.71	4.00	0.96	0.42	7.22	1.58	2.05	0.48	9.03	16.64
S2	9.77	4.64	0.94	0.41	6.73	1.59	2.18	0.53	8.64	15.54
S3	10.12	4.97	0.96	0.43	6.56	1.54	2.16	0.52	8.28	13.43
r1	7.22	3.91	1.04	0.49	5.62	1.69	2.36	0.75	167.31	333.53
r2	6.83	3.34	1.01	0.45	5.86	1.73	2.75	0.82	59.95	113.55
r3	6.90	3.34	1.02	0.47	5.77	1.72	2.70	0.80	35.76	51.71
R1	9.87	6.48	1.12	0.63	3.24	1.27	0.74	0.34	2019.58	2217.24
R2	9.65	4.72	1.25	0.66	3.06	1.25	0.79	0.35	496.94	377.52
R3	11.13	7.93	1.27	0.54	3.25	1.28	0.83	0.35	114.15	103.57

Note. In the above, rms denotes the root-mean-square, which is same as the standard deviation.

kurtosis are the characteristic parameters that reflect the symmetry and the steepness of all values of the probability density distribution curve, respectively. The expressions are shown as

$$SK = \frac{1}{n-1}\sum_{i=1}^{n}\left(f_i - \bar{f}\right)^3 / SD^3, \tag{27}$$

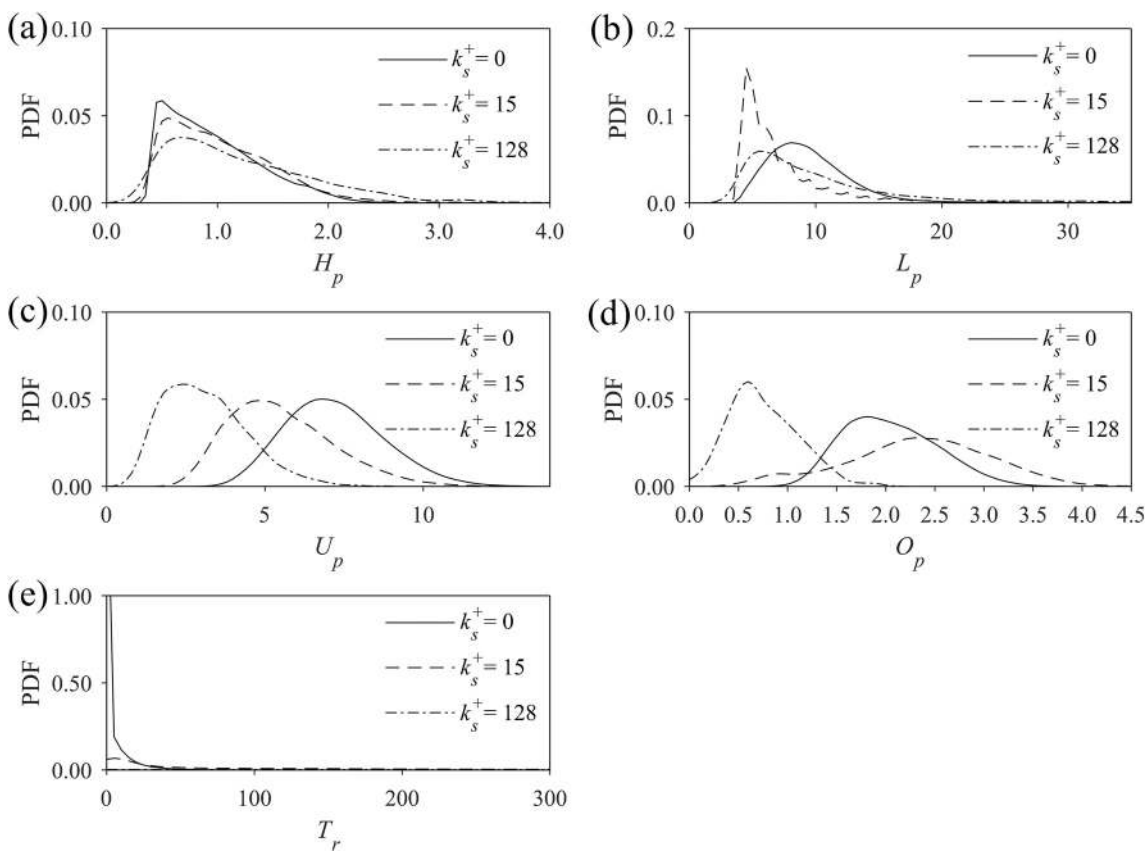

Figure 9. Probability density function (PDF) of dimensionless saltation parameters of bedload particles above the three beds (cases S0 ($k_s^+ = 0$), r0 ($k_s^+ = 15$), and R0 ($k_s^+ = 128$)) for particle spatial density $\varphi = 1.3\%$. (a) Saltation length L_p, (b) saltation height H_p, (c) particle velocity U_p, (d) angular velocity O_p, and (e) resting time T_r.

Table 7
Coefficients of Skewness and Kurtosis for S1 Case

Parameters	L_p	H_p	U_p	O_p	T_r
SK	3.041	0.831	0.399	0.374	4.884
KU	21.265	0.156	0.040	0.278	39.410

$$KU = \frac{1}{n-1}\sum_{i=1}^{n}\left(f_i - \bar{f}\right)^4 / SD^4 - 3, \tag{28}$$

where n is the number of samples, f_i and $\bar{f}$ are those saltation parameters that are required to analyze and theirs average value, respectively, and SD is the standard deviation of them. Hence, when SK approaches to 0, it shows that the data obey normal distribution. The positive skewness coefficient ($SK > 0$) signifies a left deviation, while the negative skewness coefficient ($SK < 0$) specifies a right deviation. A kurtosis coefficients of 0 indicate that the overall data distribution has the same steepness as the normal distribution. The positive kurtosis coefficient ($KU > 0$) means that the overall data distribution has sharp peak being steeper than the normal distribution, while the negative kurtosis coefficient ($KU < 0$) means data distribution has a flat peak as compared to the normal distribution.

In Table 7, the values of skewness U_p and O_p are smaller than 1.96 (significant level $\alpha = 0.05$), and the values of kurtosis approach to 0 as well, which imply that the distributions of U_p and O_p are similar than those of normal distribution. For L_p and T_r, the values of skewness and kurtosis are relatively large, as a results, their distributions show left deviations and have long tails at the right side in Figure 9. In order to further test the distributional features of a typical distribution, histograms of computational data of L_p for S1 case, U_p for S1 and R1 cases, and T_r for S1 case compared with corresponding fitted distributions are represented in Figures 10a–10d. Histogram of L_p for S1 case fits the gamma distribution and the expression is follows:

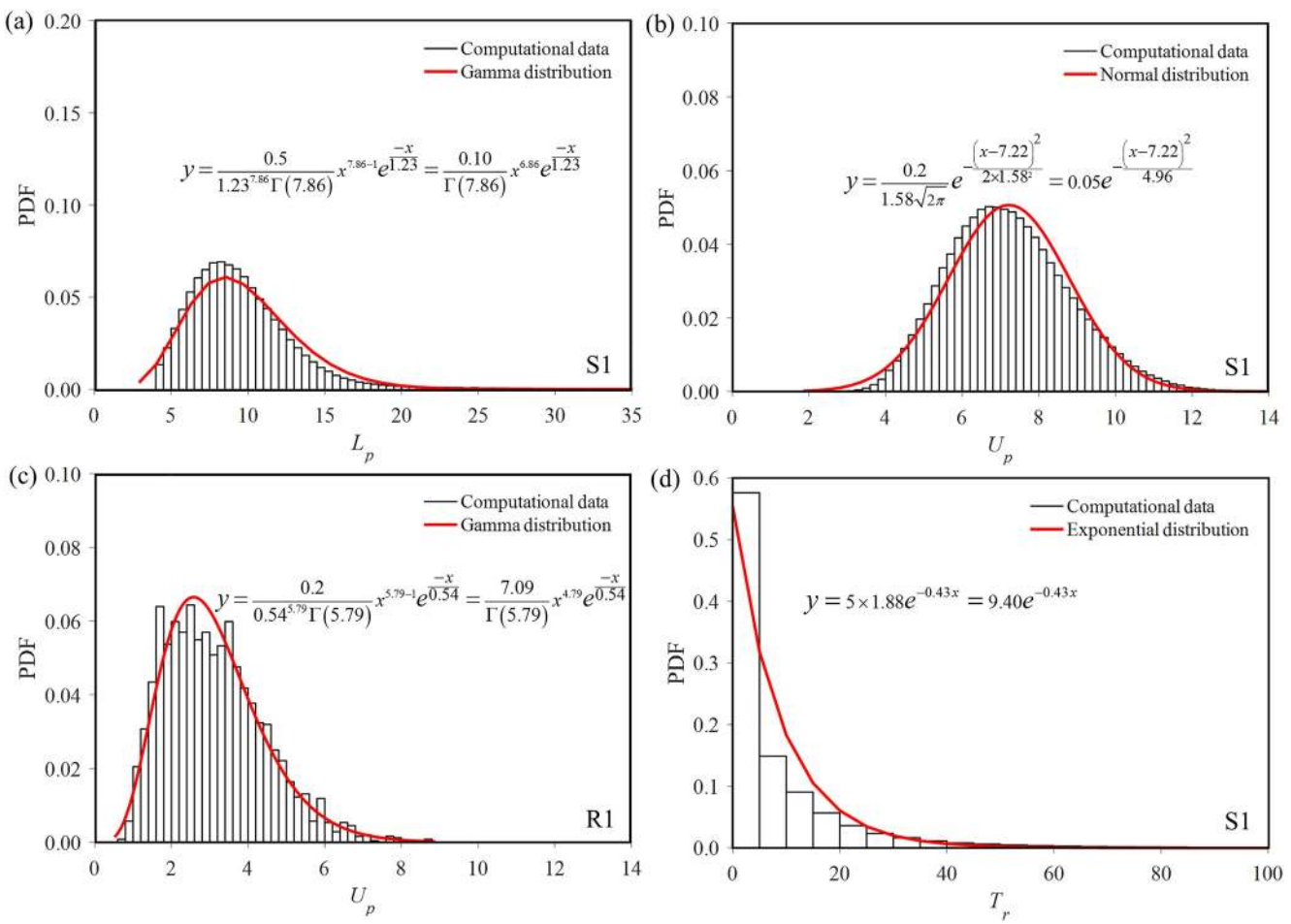

Figure 10. Histograms of typical computational data compared with corresponding fitted distributions. (a) L_p for S1 case, (b) U_p for S1 case, (c) U_p for R1 case, and (d) T_r for S1 case.

$$y = \frac{0.10}{\Gamma(7.86)} x^{6.86} e^{-x/1.23}, \quad \text{where } \Gamma(x) = \int_0^\infty e^{-t} t^{x-1} dt, \tag{29}$$

where η is the dummy variable for integration. The distributions of U_p transfer from a symmetric normal distribution for S1 case to an asymmetrical gamma distribution for R1 case. The expressions read

$$y = 0.05 e^{-(x-7.22)^2/4.96}, \tag{30}$$

$$y = \frac{7.09}{\Gamma(5.79)} x^{4.79} e^{-x/0.54}, \tag{31}$$

The histogram of computational T_r fits exponential distribution for which the expression is

$$y = 9.40 e^{-0.43x}, \tag{32}$$

Combined with Figure 9, those observations could be obtained. The PDF curve of the dimensionless saltation height decreases linearly, and the kurtosis of the PDF of H_p decreases, as the roughness increases from $k_s^+ = 0$ to $k_s^+ = 128$. For the dimensionless saltation length (where very small values of less than four have been omitted from the analysis), the PDF curve follows a gamma distribution for all three beds. However, the maximum value of the PDF of L_p decreases, as the roughness increases, which implies that the saltation length is hindered by the bed roughness; the mean value of L_p also decreases. Comparing the results from two rough beds, the kurtosis decreases slightly, as the bed roughness increases. This implies that the distribution of L_p becomes slightly more even. For the dimensionless saltation particle velocity, the distributions change from a symmetric normal distribution for the smooth bed ($k_s^+ = 0$) to an asymmetrical gamma distribution for the rough beds ($k_s^+ = 15$ and 128), which is in line with the findings of Lee et al. (2006). The skewness also increases, as the bed roughness increases. However, in previous studies, it has been suggested that the distribution of U_p is exponential (Lajeunesse et al., 2010). It is attributed to the fact that the particle velocities over mobile beds were measured to move more slowly than the present fix-bed particles. For the dimensionless angular velocity, which has so far received inadequate attention, the distribution is similar to the normal distribution; however, the distributions appear to have no deterministic relationship with the bed roughness. The kurtosis decreases slightly, as the roughness Reynolds number k_s^+ increases from 0 to 15. Moreover, the mean dimensionless angular velocity decreases, as the kurtosis increases, and the dimensionless angular velocity decreases sharply as k_s^+ increases from 15 to 128. The dimensionless resting time follows an exponential distribution, which is in agreement with the power-law distribution given by Fraccarollo and Hassan (2019). However, as the roughness Reynolds number k_s^+ increases, the maximum value of the PDF of T_r decreases and the tails of them become longer (Figures 11a–11c), suggesting that the bed roughness leads to an increase in the overall resting time of the saltating particles. Owing to the high intermittency in the saltating particle motion, the saltation of bed particles becomes more discontinuous in rough beds.

In order to examine the effects of bed roughness on the flow intensity, the simulated results for k_s^+ versus $1/\Theta$ are plotted in Figure 12 and compared with the experimental data of Rahman and Webster (2005). Those two lines do not overlap, because there are some other flow conditions, such as flow depth, which can affect the flow intensity. However, they follow a similar trend that an increase in the roughness Reynolds number reduces the overall flow intensity.

5. Discussion

In this study, a numerical model is used for simulations of bedload particle saltation. Turbulent flow is solved by the LES model, and the trajectories and states of bedload particles have been obtained by calculating forces acting considering particle-wall collision. The boundary of the bed can be set as smooth or rough in a specific simulation. Hence, it can be utilized for different flow regimes.

The main contribution of this study is successfully simulating the bedload particle movement in hydraulically smooth, transitional, and fully rough flow regimes. Response of flow and particle saltating parameters to bed roughness reflects that the effects of bed roughness on the transport of bedload has been detected. The double-averaged flow streamwise velocity, Reynolds shear stress, and Reynolds normal stresses show a shift of individual

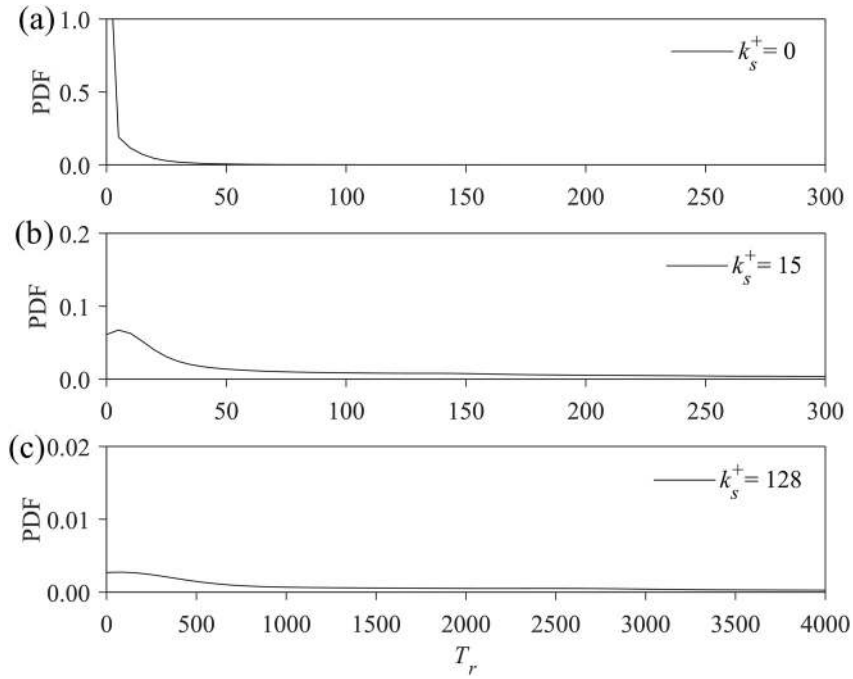

Figure 11. Detailed observation of probability density function (PDF) of bedload dimensionless resting time in three beds for particle spatial density $\varphi = 1.3\%$. (a) S1 case ($k_s^+ = 0$), (b) r1 case ($k_s^+ = 15$), and (c) R1 case ($k_s^+ = 128$).

profiles for rough beds. The results suggest that there is an obvious link between the near-bed turbulence and bedload particle saltation. The bed roughness interrupts secondary currents and coherent structures near the bed, and high-speed and low-speed streaks break into irregular small fragments and disappear. The high-speed sweeps enter from the high-momentum layers of the flow toward the bed causing bed particle motion contributing to the instability of the sand bed. In addition, sweeps are found to produce locally a low-pressure field which exerts a lift force on near-bed particles and thus sets in motion near-bed particles.

Bed roughness is found to increase the particle resting time and to decrease saltation length, velocity, and angular velocity of the particle. The kurtosis and skewness of particle characteristics are quantified and the distribution of typical saltation parameters like saltation length, particle velocity, and resting time fit well with expressions of gamma, normal, and exponential distributions, respectively. The changes of distribution due to bed roughness are observed as well, where the particle velocity transforms from a symmetrical normal to an asymmetrical gamma distribution is taken as an example to analysis.

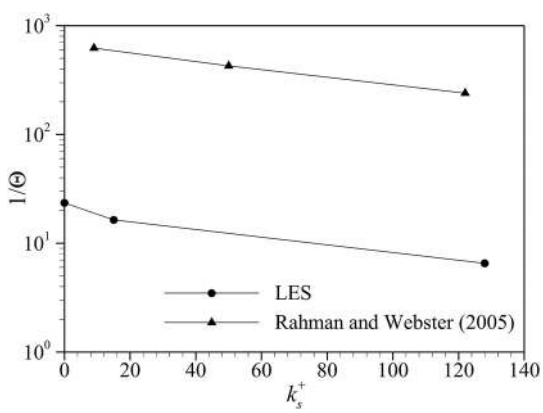

Figure 12. Roughness Reynolds number k_s^+ as a function of flow intensity function $1/\Theta$ given by the large-eddy simulation (LES) and the experimental data of Rahman and Webster (2005).

There are some limitations and also noteworthy points for the study. The first thing required to be paid attention is that the particle statistics that are obtained over the fixed bed differ from those over a mobile bed. Hence, different findings due to this setting have been highlighted. Next, parts of definitions of quantities related to particle saltation are different from parts of studies, which have been also clarified. For example, "hop length" and "saltation length" measured by various authors are totally different issues, the former means the total distance traveled by the particle between subsequent collisions with the bed, while the latter represents the distance from initiation to halting of particles. Third, there still exists some simplifications for the model such as not including particle-particle collisions. Nevertheless, the study on tendency of the particle saltating parameters for different rough beds is still of research significance.

6. Conclusions

In natural streams, the morphology of a rough bed is heterogeneous and hence flow-bed-sediment interactions are utterly complex. With the goal to clarify the influence of bed roughness on the bedload transport rate, LESs were carried out with a focus on the particle saltation characteristics of bedload transport. Bed roughness regimes included hydraulically smooth, transitional, and fully rough flow regimes.

The results of the simulations reveal that the double-averaged streamwise velocity is affected by bed roughness, resulting in a leftward shift of the velocity profiles and the slope of rough-bed velocity profiles yields the von Kármán constant. The profiles of the dimensionless Reynolds shear stress for the three beds are similar, but the distance of the peak Reynolds stress from the bed increases with an increase in bed roughness. This feature is also evident in the profiles of Reynolds normal stresses. The peak of the dimensionless Reynolds normal stresses decreases with an increase in roughness. Secondary currents appear in the channel corners in the smooth and transitional flows, but are almost absent in the fully rough flow. This is because the bed roughness disrupts the secondary currents near the bed. Coherent structures, in the form of alternating high-speed and low-speed streaks, are clearly evident over the smooth bed. However, the streaks break into irregular small fragments and gradually disappear, as the bed roughness increases.

Regarding particle saltation statistics, as the bed roughness increases, the ratio of bed shear stress to critical bed shear stress and the resting time increase, but particle saltation length, particle velocity, and particle angular velocity decrease significantly. This can be attributed to a sheltering effect of the rough bed, creating pits in which particles can hide. With regard to the saltation height, no significant change occurs, as the bed roughness increases. As the particle spatial density increases, the saltation length, saltation height, particle velocity, and angular velocity remain almost unchanged, but the resting time decreases, which may be due to increased particle-particle interaction.

The distributions of the key saltation parameters, including their changes, have been assessed using PDF curves. The saltation height, saltation length, particle angular velocity, and resting time have linear, gamma, normal, and exponential distributions, respectively. However, as the bed roughness increases, the kurtosis and skewness of some particle characteristics change and the particle velocity transforms from a symmetrical normal to an asymmetrical gamma distribution.

Data Availability Statement

Numerical data presented herein can be downloaded from the Zenodo website (http://doi.org/10.5281/zenodo.5109460).

Acknowledgments
The authors gratefully acknowledge the National Natural Science Foundation of China (No. U2040214 and 12172196) and 111 Project (No. B18031) for providing the financial support necessary to carry out this research. They also acknowledge the support from Advance Research Computing at Cardiff University and the Supercomputing Wales project, which is partially funded by the European Regional Development Fund (ERDF) via the Welsh Government.

References

Abbott, J. E., & Francis, J. R. D. (1977). Saltation and suspension trajectories of solid grains in a water stream. *Philosophical Transactions of the Royal Society of London, Series A*, *284*(1321), 225–254.
Alfonsi, G., Ferraro, D., Lauria, A., & Gaudio, R. (2019). Large-eddy simulation of turbulent natural-bed flow. *Physics of Fluids*, *31*(8), 085105.
Amir, M., Nikora, V. I., & Stewart, M. T. (2014). Pressure forces on sediment particles in turbulent open-channel flow: A laboratory study. *Journal of Fluid Mechanics*, *757*, 458–497.
Ancey, C. (2010). Stochastic modeling in sediment dynamics: Exner equation for planar bed incipient bed load transport conditions. *Journal of Geophysical Research*, *115*, F00A11. https://doi.org/10.1029/2009JF001260
Bagnold, R. A. (1966). *An approach to the sediment transport problem from general physics (Geological Survey Professional Paper 422-I)*. US Government Printing Office.
Bai, J., Fang, H. W., & Stoesser, T. (2013). Transport and deposition of fine sediment in open channels with different aspect ratios. *Earth Surface Processes and Landforms*, *38*(6), 591–600.
Barati, R., Neyshabouri, S. A. A. S., & Ahmadi, G. (2018). Issues in Eulerian-Lagrangian modeling of sediment transport under saltation regime. *International Journal of Sediment Research*, *33*(4), 441–461.
Berzi, D., & Fraccarollo, L. (2016). Intense sediment transport: Collisional to turbulent suspension. *Physics of Fluids*, *28*(2), 023302.
Bialik, R. J. (2011). Particle-particle collision in Lagrangian modelling of saltating grains. *Journal of Hydraulic Research*, *49*(1), 23–31.
Bombardelli, F. A., González, A. E., & Niño, Y. I. (2008). Computation of the particle Basset force with a fractional-derivative approach. *Journal of Hydraulic Engineering*, *134*(10), 1513–1520.
Brown, P. P., & Lawler, D. F. (2003). Sphere drag and settling velocity revisited. *Journal of Environmental Engineering*, *129*(3), 222–231.
Bui, V. H., Bui, M. D., & Rutschmann, P. (2019). Advanced numerical modeling of sediment transport in gravel-bed rivers. *Water*, *11*(3), 550.
Cevheri, M., McSherry, R., & Stoesser, T. (2016). A local mesh refinement approach for large-eddy simulations of turbulent flows. *International Journal for Numerical Methods in Fluids*, *82*(5), 261–285.
Chan-Braun, C., García-Villalba, M., & Uhlmann, M. (2011). Force and torque acting on particles in a transitionally rough open-channel flow. *Journal of Fluid Mechanics*, *684*, 441–474.

Chua, V. K., Fraga, B., Stoesser, T., Hong, S., & Sturm, T. (2019). Effect of bridge abutment length on turbulence structure and flow through the opening. *Journal of Hydraulic Engineering*, *145*(6), 04019024.
Crowe, C. T., Sommerfeld, M., & Tsuji, M. (1998). *Multiphase flow with droplets and particles*. CRC Press.
Daitche, A. (2013). Advection of inertial particles in the presence of the history force: Higher order numerical schemes. *Journal of Computational Physics*, *254*, 93–106.
Dey, S. (2014). *Fluvial hydrodynamics: Hydrodynamic and sediment transport phenomena*. Springer-Verlag.
Dey, S., Ali, S. K., & Padhi, E. (2020). Hydrodynamic lift on sediment particles at entrainment: Present status and its prospect. *Journal of Hydraulic Engineering*, *146*(6), 03120001.
Donahue, C. M., Hrenya, C. M., Davis, R. H., Nakagawa, K. J., Zelinskaya, A. P., & Joseph, G. G. (2010). Stokes' cradle: Normal three-body collisions between wetted particles. *Journal of Fluid Mechanics*, *650*, 479–504.
Durán, O., Andreotti, B., & Claudin, P. (2012). Numerical simulation of turbulent sediment transport, from bed load to saltation. *Physics of Fluids*, *24*(10), 103306.
Einstein, H. A. (1941). Formulas for the transportation of bed load. *Transactions of the American Society of Civil Engineers*, *107*, 561–597.
Fang, H. W., Lai, H. J., Cheng, W., Huang, L., & He, G. J. (2017). Modeling sediment transport with an integrated view of the biofilm effects. *Water Resources Research*, *53*(9), 7536–7557. https://doi.org/10.1002/2017WR020628
Fathel, S. L., Furbish, D. J., & Schmeeckle, M. W. (2015). Experimental evidence of statistical ensemble behavior in bed load sediment transport. *Journal of Geophysical Research: Earth Surface*, *120*(11), 2298–2317. https://doi.org/10.1002/2015JF003552
Forooghi, P., Stroh, A., Schlatter, P., & Frohnapfel, B. (2018). Direct numerical simulation of flow over dissimilar, randomly distributed roughness elements: A systematic study on the effect of surface morphology on turbulence. *Physical Review Fluids*, *3*(4), 44605.
Fraccarollo, L., & Hassan, M. A. (2019). Einstein conjecture and resting-time statistics in the bed-load transport of monodispersed particles. *Journal of Fluid Mechanics*, *876*, 1077–1089.
Fraga, B., & Stoesser, T. (2016). Influence of bubble size, diffuser width, and flow rate on the integral behavior of bubble plumes. *Journal of Geophysical Research: Oceans*, *121*(6), 3887–3904. https://doi.org/10.1002/2015JC011381
Glowinski, R., Pan, T. W., Hesla, T. I., Joseph, D. D., & Jacques, P. (1999). A distributed Lagrange multiplier/fictitious domain method for particulate flows. *International Journal for Numerical Methods in Fluids*, *30*(8), 1043–1066.
Gordon, R., Carmichael, J. B., & Isackson, F. J. (1972). Saltation of plastic balls in a 'one-dimensional' flume. *Water Resources Research*, *8*(2), 444–459.
Hill, K., Dellangelo, L., & Meerschaert, M. M. (2010). Heavy-tailed travel distance in gravel bed transport: An exploratory enquiry. *Journal of Geophysical Research*, *115*, F00A14. https://doi.org/10.1029/2009JF001276
Hohermuth, B., & Weitbrecht, V. (2018). Influence of bed-load transport on flow resistance of step-pool channels. *Water Resources Research*, *54*(8), 5567–5583. https://doi.org/10.1029/2017WR021523
Huang, L., Fang, H., & Reible, D. (2015). Mathematical model for interactions and transport of phosphorus and sediment in the three gorges reservoir. *Water Research*, *85*, 393–403.
Ji, C. N., Munjiza, A., Avital, E., Xu, D., & Williams, J. (2014). Saltation of particles in turbulent channel flow. *Physical Review E*, *89*(5), 052202.
Joseph, G. G., & Hunt, M. L. (2004). Oblique particle–wall collisions in a liquid. *Journal of Fluid Mechanics*, *510*, 71–93.
Kempe, T., & Fröhlich, J. (2012). Collision modelling for the interface-resolved simulation of spherical particles in viscous fluids. *Journal of Fluid Mechanics*, *709*, 445–489.
Kharlamova, I. S., & Vlasák, P. (2015). Model of rough bed for numerical simulation of saltation. *European Journal of Environmental and Civil Engineering*, *19*(3), 366–385.
Khosronejad, A., Kang, S., Farhadzadeh, A., & Sotiropoulos, F. (2020). On the genesis and evolution of barchan dunes: Hydrodynamics. *Physics of Fluids*, *32*(8), 086602.
Khosronejad, A., & Sotiropoulos, F. (2014). Numerical simulation of sand waves in a turbulent open channel flow. *Journal of Fluid Mechanics*, *753*, 150–216.
Khosronejad, A., & Sotiropoulos, F. (2017). On the genesis and evolution of barchan dunes: Morphodynamics. *Journal of Fluid Mechanics*, *815*, 117–148.
Kidanemariam, A. G., & Uhlmann, M. (2014). Direct numerical simulation of pattern formation in subaqueous sediment. *Journal of Fluid Mechanics*, *750*, R2.
Krecic, M. R., & Hanes, D. M. (1996). *An analysis of particle saltation dynamics*. Paper 826 presented at 25th Conference on Coastal Engineering, Orlando, Florida (pp. 3846–3859).
Kuerten, J. G. (2016). Point-particle DNS and LES of particle-laden turbulent flow-a state-of-the-art review. *Flow, Turbulence and Combustion*, *97*(3), 689–713.
Lajeunesse, E., Malverti, L., & Charru, F. (2010). Bed load transport in turbulent flow at the grain scale: Experiments and modeling. *Journal of Geophysical Research*, *115*, F04001. https://doi.org/10.1029/2009JF001628
Lee, H., & Balachandar, S. (2017). Effects of wall roughness on drag and lift forces of a particle at finite Reynolds number. *International Journal of Multiphase Flow*, *88*, 116–132.
Lee, H., Ha, M. Y., & Balachandar, S. (2011). Rolling/sliding of a particle on a flat wall in a linear shear flow at finite Re. *International Journal of Multiphase Flow*, *37*(2), 108–124.
Lee, H. Y., Chen, Y. H., You, J. Y., & Lin, Y. T. (2000). Investigations of continuous bedload saltating process. *Journal of Hydraulic Engineering*, *126*(9), 691–700.
Lee, H. Y., & Hsu, I. S. (1994). Investigation of saltating particle motions. *Journal of Hydraulic Engineering*, *120*(7), 831–845.
Lee, H. Y., Lin, Y. T., Yunyou, J., & Wenwang, H. (2006). On three-dimensional continuous saltating process of sediment particles near the channel bed. *Journal of Hydraulic Research*, *44*(3), 374–389.
Liu, D. T., Liu, X. F., & Fu, X. D. (2019). LES-DEM simulations of sediment saltation in a rough-wall turbulent boundary layer. *Journal of Hydraulic Research*, *57*(6), 786–797.
Liu, Y., Stoesser, T., Fang, H. W., Papanicolaou, A., & Tsakiris, A. G. (2017). Turbulent flow over an array of boulders placed on a rough permeable bed. *Computers & Fluids*, *158*, 120–132.
Lukerchenko, N. (2010). Discussion of "computation of the particle basset force with a fractional-derivative approach" by F. A. Bombardelli, A. E. González, and Y. I. Niño. *Journal of Hydraulic Engineering*, *136*(10), 853–854.
Lukerchenko, N., Kvurt, Y., Keita, I., Chara, Z., & Vlasak, P. (2012). Drag force, drag torque, and Magnus force coefficients of rotating spherical particle moving in fluid. *Particulate Science and Technology*, *30*(1), 55–67.
Maldonado, S., & Borthwick, A. G. (2014). Sensitivity analysis and statistical convergence of a saltating particle model. *Journal of Hydraulic Engineering*, *141*(5), 04014091.

Maurin, R., Chauchat, J., & Frey, P. (2018). Revisiting slope influence in turbulent bedload transport: Consequences for vertical flow structure and transport rate scaling. *Journal of Fluid Mechanics*, *839*, 135–156.
Mazzuoli, M., Blondeaux, P., Vittori, G., Uhlmann, M., Simeonov, J., & Calantoni, J. (2020). Interface-resolved direct numerical simulations of sediment transport in a turbulent oscillatory boundary layer. *Journal of Fluid Mechanics*, *885*, A28.
Mazzuoli, M., & Uhlmann, M. (2017). Direct numerical simulation of open-channel flow over a fully rough wall at moderate relative submergence. *Journal of Fluid Mechanics*, *824*, 722–765.
McLaughlin, M. H. (1968). *An experimental study of particle-wall collision relating to flow of solid particles in fluid*(Doctoral dissertation). California Institute of Technology.
McSherry, R., Chua, K., Stoesser, S., & Mulahasan, S. (2018). Free surface flow over square bars at intermediate relative submergence. *Journal of Hydraulic Engineering*, *56*(6), 825–843.
Meunier, P., Métivier, F., Lajeunesse, E., Meriaux, A., & Faure, J. (2006). Flow pattern and sediment transport in a braided river: The "torrent de St Pierre" (French Alps). *Journal of Hydrology*, *330*(3–4), 496–505.
Nezu, I., & Nakagawa, H. (1993). *Turbulence in open-channel flows*. Balkema.
Nicoud, F., & Ducros, F. (1999). Subgrid-scale stress modelling based on the square of the velocity gradient tensor. *Flow, Turbulence and Combustion*, *62*(3), 183–200.
Nikora, V. (2005). Flow turbulence over mobile gravel-bed: Spectral scaling and coherent structures. *Acta Geophysica Polonica*, *53*(4), 539–552.
Nikora, V., Goring, D., McEwan, I., & Griffiths, G. (2001). Spatially averaged open-channel flow over rough bed. *Journal of Hydraulic Engineering*, *127*(2), 123–133.
Niño, Y., & García, M. (1998). Experiments on saltation of sand in water. *Journal of Hydraulic Engineering*, *124*(10), 1014–1025.
Ouro, P., Fraga, B., Lopez-Novoa, U., & Stoesser, T. (2019). Scalability of an Eulerian-Lagrangian large-eddy simulation solver with hybrid MPI/OpenMP parallelisation. *Computers & Fluids*, *179*, 123–136.
Ouro, P., & Stoesser, T. (2019). Impact of environmental turbulence on the performance and loadings of a tidal stream turbine. *Flow, Turbulence and Combustion*, *102*(3), 613–639.
Pähtz, T., Clark, A. H., Valyrakis, M., & Durán, O. (2020). The physics of sediment transport initiation, cessation, and entrainment across aeolian and fluvial environments. *Reviews of Geophysics*, *58*, e2019RG000679. https://doi.org/10.1029/2019RG000679
Pähtz, T., & Durán, O. (2020). Unification of aeolian and fluvial sediment transport rate from granular physics. *Physical Review Letters*, *124*(16), 168001.
Papanicolaou, A. T. N., Elhakeem, M., Krallis, G., Prakash, S., & Edinger, J. (2008). Sediment transport modeling review current and future developments. *Journal of Hydraulic Engineering*, *134*(1), 1–14.
Pitlick, J., & Van Steeter, M. M. (1998). Geomorphology and endangered fish habitats of the upper Colorado river: 2. Linking sediment transport to habitat maintenance. *Water Resources Research*, *34*(2), 303–316.
Rahman, S., & Webster, D. R. (2005). The effect of bed roughness on scalar fluctuations in turbulent boundary layers. *Experiments in Fluids*, *38*(3), 372–384.
Rodi, W., Constantinescu, G., & Stoesser, T. (2013). *Large-eddy simulation in hydraulics*. CRC Press, Taylor & Francis Group.
Roma, A. M., Peskin, C. S., & Berger, M. J. (1999). An adaptive version of the immersed boundary method. *Journal of Computational Physics*, *153*(2), 509–534.
Roseberry, J. C., Schmeeckle, M. W., & Furbish, D. J. (2012). A probabilistic description of the bed load sediment flux: 2. Particle activity and motions. *Journal of Geophysical Research*, *117*, F03032. https://doi.org/10.1029/2012JF002353
Sawatzki, O. (1970). Das Strömungsfeld um eine rotierende Kugel. *Acta Mechanica*, *9*(3–4), 159–214.
Schiller, L., & Naumann, A. (1935). A drag coefficient correlation. *Zeitschrift des Vereins Deutscher Ingenieure*, *77*, 318–320.
Schmeeckle, M. W. (2014). Numerical simulation of turbulence and sediment transport of medium sand. *Journal of Geophysical Research: Earth Surface*, *119*, 1240–1262. https://doi.org/10.1002/2013JF002911
Schmeeckle, M. W., Nelson, J. M., Pitlick, J., & Bennett, J. P. (2001). Interparticle collision of natural sediment grains in water. *Water Resources Research*, *37*(9), 2377–2391.
Shim, J., & Duan, J. G. (2017). Experimental study of bed-load transport using particle motion tracking. *International Journal of Sediment Research*, *32*(1), 73–81.
Stoesser, T. (2010). Physically realistic roughness closure scheme to simulate turbulent channel flow over rough beds within the framework of LES. *Journal of Hydraulic Engineering*, *136*(10), 812–819.
Stoesser, T., McSherry, R., & Fraga, B. (2015). Secondary currents and turbulence over non-uniformly roughened open-channel bed. *Water*, *7*(9), 4896–4913.
Stokes, G. G. (1851). *On the effect of the internal friction of fluids on the motion of pendulums* (Vol. 9, pp. 8). Pitt Press.
Swamee, P. K., & Ojha, C. S. P. (1991). Drag coefficient and fall velocity of nonspherical particles. *Journal of Hydraulic Engineering*, *117*(5), 660–667.
Van Hinsberg, M. A. T., ten Thije Boonkkamp, J. H. M., & Clercx, H. J. (2011). An efficient, second order method for the approximation of the Basset history force. *Journal of Computational Physics*, *230*(4), 1465–1478.
Vanoni, V. A. (1975). *Sedimentation engineering (ASCE manual number 54)*. American Society of Civil Engineers.
van Rijn, L. C. (1984). Sediment transport, Part I: Bed load transport. *Journal of Hydraulic Engineering*, *110*(10), 1431–1456.
Vowinckel, B., Jain, R., Kempe, T., & Fröhlich, J. (2016). Entrainment of single particles in a turbulent open-channel flow: A numerical study. *Journal of Hydraulic Research*, *54*(2), 158–171.
Vowinckel, B., Kempe, T., & Fröhlich, J. (2014). Fluid-particle interaction in turbulent open channel flow with fully-resolved mobile beds. *Advances in Water Resources*, *72*, 32–44.
Wiberg, P. L., & Smith, J. D. (1985). A theoretical model for saltating grains in water. *Journal of Geophysical Research*, *90*(C4), 7341–7354.
Wiberg, P. L., & Smith, J. D. (1987). Calculations of the critical shear stress for motion of uniform and heterogeneous sediments. *Water Resources Research*, *23*(8), 1471–1480.
Witz, M., Cameron, S. M., & Nikora, V. (2019). Bed particle dynamics at entrainment. *Journal of Hydraulic Research*, *57*(4), 464–474.
Wu, Z., Furbish, D., & Foufoula-Georgiou, E. (2020). Generalization of hop distance-time scaling and particle velocity distributions via a two-regime formalism of bedload particle motions. *Water Resources Research*, *56*, e2019WR025116. https://doi.org/10.1029/2019WR025116
Yousefi, A., Costa, P., & Brandt, L. (2020). Single sediment dynamics in turbulent flow over a porous bed—Insights from interface-resolved simulations. *Journal of Fluid Mechanics*, *893*, A24.
Yuan, J., & Piomelli, U. (2014). Roughness effects on the Reynolds stress budgets in near-wall turbulence. *Journal of Fluid Mechanics*, *760*, R1.
Zhao, C. W., Fang, H. W., Liu, Y., Dey, S., & He, G. J. (2020). Impact of particle shape on saltating mode of bedload transport sheared by turbulent flow. *Journal of Hydraulic Engineering ASCE*, *146*(5), 04020034.